The University Of Sheffield.

Next generation avalanche photodiodes: realising new potentials using nm wide avalanche regions

By:

Manuel A. Moreno

A thesis submitted in partial fulfilment of the requirements for the degree of Master of Philosophy

The University of Sheffield
Department of Electronic and Electrical Engineering
Semiconductor Materials and Devices Group

Submission Date 27/07/2016

Abstract

Each year, the flow of Internet data around the world increases exponentially. Therefore, each year, telecommunication companies must improve data management and develop new high speed optical network components. In non-coherent detection, InGaAs p-i- n diodes are used in the detector modules for 40 to 100 GB/s networks.

Sparate Absorption-Multiplication (SAM) avalanche photodiodes are a major improvemnent from p-i-n diodes, in which light absorption and avalanche gain occurs in different parts of the APDs. Unfortunately, commercial SAM APDs employing InGaAs/InP, and more recently InGaAs/InAlAs, are unable to provide sufficient bandwidth with appreciable gain at 40 Gb/s and higher. This is due to their low gain-bandwidth product (GBP).

SAM APDs with w < 50 nm and negligible tunnelling current can potentially raise the GBP from 200 GHz to 1 THz, boosting the performance of next-generation Tb/s Direct Detection systems. A new wide-band gap material, AlAsSb, has been chosen as a suitable candidate to replace InAlAs.

In this thesis is summarised data taken from Al1-xGaxAs0.56Sb0.44 (x = 0, 0.05, 0.1, + + 0.15) p i n diode structures. It is included all results obtained for I-V, C-V, avalanche gain, spectral response, and temperature dependence of avalanche breakdown. Also, is presented a study of several alternatives when carrying out the mesa step fabrication process, in order to achieve uniform avalanche gain across a given sample.

Glossary of terms

hv	Photon energy
Eg	Energy bandgap
λ	Wavelength
λc	Cutoff wavelength
APD	Avalanche photodiode
SAM	Separate absorption multiplication
F	Excess noise factor
M	Multiplication factor
k	Ionisation coefficient ratio
k_{eff}	Effective ionisation coefficient ratio
α	Electron ionisation coefficient
β	Hole ionisation coefficient
w	Avalanche region width
PDF	Probability distribution function
BRC	RC limited bandwidth
t_{r}	Transit time
B_{tr}	Transit time limited bandwidth
τ_{diff}	Diffusion time
B_{diff}	Diffusion time limited bandwidth
GBP	Gain bandwidth product
IV	Current-voltage
CV	Capacitance-voltage
a	Absorption coefficient
P	Optical power
R	Reflectivity
R_{vT}	Theoretical responsivity
R_{vm}	Measured responsivity
E_{the}	Ionisation threshold energy for electron
E_{thh}	Ionisation threshold energy for hole
E	Electric field
M_{e}	Pure electron initiated gain

M_h	Pure hole initiated gain
C_{bd}	Temperature coefficient of breakdown voltage
V_{bd}	Breakdown voltage
T	Temperature
N_i	Mean square noise current
N_c	Corrected noise power
N_M	Measured noise power
B	Effective noise bandwidth
I_{pr}	Primary current
d_e	Dead space for electron
d_h	Dead space for hole
q	Electron charge
C_j	Junction capacitance
ε_o	Vacuum permitivity
ε_r	Dielectric constant
d_w	Depletion width
A	Device area
n	Ideality factor
I_d	Dark current
I_o	Saturation current
k_B	Boltzmann’s constant
R_s	Series Resistance
I_{tunn}	Tunnelling current
m^*	Effective electron mass
h	Plank’s constant
V	Applied voltage
SMU	Source measure unit
AC	Alternating current
DC	Direct current
LIA	Lock-in Amplifier
J_{gr}	Generation recombination current density
J_d	Diffusion current density
L_0	Diffusion length of minority carrier

θ_{sig}	Phase of measured signal
θ_{ref}	Phase of reference signal
I_{ph}	Photocurrent
TIA	Transimpedence amplifier
TLM	Transmission line model
R_{sys}	System resistance
R_c	Contact resistance
$R_{semiconductor}$	Semiconductor resistance
DUT	Device under Test
MBE	Molecular beam epitaxy
d	Diameter
SEM	Scanning electron microscopy
ICP	Inductive coupled plasma
BCB	B-staged bisbenzocyclobutene
SI	Semi-insulating
ΔE_c	Conduction band discontinuity
k_s	Gradient of noise power versus photocurrent
SPAD	Single photon avalanche diode
N	Phonon occupation number

Contents

1. Introduction

1.1 Background

Photodetectors are an important class of optoelectronic devices that play an essential role in many applications, such as CCD cameras, barcode scanners and position sensors. The electronic properties of photodetectors, such as photocurrent in a photoconductor or photovoltage in a photovoltaic detector, undergo change as a result of incident light. The functioning of a photodiode entails three stages:

a) Generation of free carriers due to incident light.
b) Movement of the free carriers, and possibly some current-gain mechanism, giving rise to photocurrent.
c) Interaction between the photocurrent and an external circuit to provide an output signal.

Most commercial photodetectors consist of semiconductors, such as photodiodes and phototransistors. In a photodiode, photons that have been absorbed in the semiconductor are converted in electro-hole pairs. These photo-generated carriers are then accelerated by an electric field within the photodiode, producing a current through it. The current is proportional to incident optical power. On the other hand, phototransistors usually take the form of a bipolar transistor that employs light to generate a photocurrent, using the internal transistor's current gain h_{fe} to amplify the generated photocurrent.

The energy band gap(s), E_g, of the semiconductor(s) employed within the photodiodes determines the wavelength range of the light to which they will respond. E_g can vary from a few eV down to several meV. By using different semiconductor materials, it is possible to produce photodiodes sensitive to different ranges of light, from deep UV to far infrared. For example, semiconductors like Si, Ge, GaAs, InP, InGaAs, AlGaAs and InAlAs has been widely used to fabricate commercial photodiodes.

1.2 Avalanche photodiodes (APDs)

It is possible to incorporate some form of gain mechanism into the photodiode to increase the photo-generated current. External amplifiers can usually provide a certain amount of gain, but this is at the expense of reduced signal to noise ratio for the overall detection system in those cases where the optical signal has a low input power. Where the system requires high amplification of the signal, avalanche photodiodes (APDs) can provide this via their avalanche gains, which are the end result of successive impact ionisation events.

In an impact ionisation event, a carrier travelling along a high electric field gains enough energy to enable it, upon collision with lattice atoms, to release a portion of its energy to promote an electron from the valence band to the conduction band, generating a new electron-hole pair. Impact ionisation coefficients, α for electron and β for holes, are often used to quantify the impact ionisation properties of different materials, where α (or β) is defined as the average distance that an electron (or hole) travels along the electric field before it initiates an impact ionization event.

Since the 1960s, several mathematical models have been put forward to calculate various avalanche gain related parameters using impact ionisation coefficients, with different assumptions of the impact ionisation process. One of the most commonly used models to describe the impact ionization mechanism is the “Local model” [1]. In this case, the impact ionisation coefficient depends exclusively on the local electrical field applied. The Random Path Length (RPL) [2] is a more recent model that allows for the use of the dead space. It is defined as the minimum distance that a carrier must travel before the probability of it initiating an impact ionisation event becomes non-zero. Including dead space in the calculations of avalanche gain related parameters becomes important where the dead space represents a significant fraction of the avalanche region width.

1.3 Motivation for the project

Researchers have tried to improve APD performance by employing semiconductors with a large α and β ratio (α/β) [1] for avalanche regions in APDs, in order to achieve low avalanche noise. Therefore, Si (α/β ~ 100) APDs have become predominant. Over the course of the last ten years, other materials, such as HgCdTe [3] and InAs [4] APDs, have demonstrated very low excess noise at high gains. However, due to their narrow band gaps, 056 eV and 0.35 eV respectively, they need to work at low operating temperatures, typically between - 20°C and -90°C, in order to suppress their high dark current.

In addition to using materials with a high α/β ratio, it is also possible to achieve low excess noise by employing very narrow avalanche regions. As the avalanche region narrows, APD bandwidth increases and excess noise decreases [5]. Nevertheless, for each material there is a lower limit on the width of the avalanche region, as tunnelling current becomes more prominent. This limit is largely dependent on the material's band gap. The key is therefore to employ materials with the largest possible E_g for the avalanche region, in order to mitigate the avalanche region width limit imposed by tunnelling current.

AlAsSb is lattice matched to InP substrate and demonstrates low excess noise approaching the levels found in Si APDs, with k_{eff} ~ 0.05 in a 230 nm p-i-n homojunction [6]. An InGaAs/AlAsSb SAM APD incorporating a 40 nm AlAsSb multiplication layer evidenced k_{eff} ~ 0.15, slightly lower than an InGaAs/InAlAs APD with w of 100 nm [7]. This represents better excess noise performance than commercial low noise InGaAs/InP APDs, whilst not reaching the levels of InAs and Si APDs. Thus, InGaAs/AlAsSb SAM APDs adopting very thin multiplication regions prove promising for high speed operation.

1.3.1 APDs for the bandwidth demanded by Internet traffic

Each year, the flow of Internet data around the world increases exponentially. Cisco Visual Networking Index predicted that annual global Internet data traffic would

reach 966 exabytes by 2015 [8]. Therefore, each year, telecommunication companies must improve data management and develop new high speed optical network components.

There are two basic schemes for network receivers: coherent detection and non-coherent detection. Coherent detection employs a local oscillating signal that mixes with the incoming signal to improve input detection. This type of receiver has been successfully adopted for telecommunication in the 40 to 100 Gb/s range. In contrast, non-coherent detection receivers are less complex and cheaper and are predominately used for low bit-rate modules. In non-coherent detection, InGaAs p-i-n diodes are used in the detector modules for 40 to 100 GB/s networks [9].

A major limitation of InGaAs p-i-n diodes is that the absorption layer thickness has to be reduced in order to achieve a high bandwidth. Such reduction degrades the receiver sensitivity as less optical signal is absorbed in the diode. One method of solving this problem is to employ Separate Absorption-Multiplication (SAM) avalanche photodiodes, in which light absorption and avalanche gain occurs in different parts of the APDs. By using InGaAs as the absorption layer and InP as the avalanche region, receiver sensitivity is enhanced whilst bandwidth is maintained. Unfortunately, SAM APDs employing InGaAs/InP, and more recently InGaAs/InAlAs, are unable to provide sufficient bandwidth with appreciable gain at 40 Gb/s and higher. This is due to their low gain-bandwidth product (GBP), which is typically below 200 GHz [10, 11]. It is possible to increase GBP by reducing multiplication thickness, w; however, where w becomes too thin, the band-to-band tunnelling increases overall APD dark current significantly, as previously discussed. For InP and InAlAs, this lower limit are considered to be ~ 150 nm [12].

APDs with $w < 50$ nm and negligible tunnelling current can potentially raise the GBP from 200 GHz to 1 THz, boosting the performance of next-generation Tb/s Direct Detection systems. A new wide-band gap material, AlAsSb, has been chosen as a suitable candidate to replace InAlAs. AlAsSb is lattice matched to InP substrates and boasts an indirect bandgap of 1.65 eV, which is larger than the direct bandgaps of 1.34 eV and 1.45 eV found in InP and InAlAs, respectively. Its phonon assisted

tunnelling process can be expected to exhibit a lower band-to-band tunnelling current and a smaller temperature coefficient of breakdown voltage, Cbd = ΔVbd/ΔT, where ΔVbd and ΔT are the breakdown voltage and temperature differences.

Furthermore, it has been proven that InGaAs/AlAsSb SAM APD with *w* = 40nm exhibits excess noise that is slightly lower than an InGaAs/AnAlAs APD with *w* = 100nm [13]. In this thesis, AlAsSb APDs will be investigated.

1.4 Overview of the report

Chapter 2 presents all background theory employed when analysing the experimental results of the AlAsSb devices, taking in avalanche gain, impact ionisation coefficient, temperature dependence of avalanche breakdown, excess noise, gain-bandwidth product, and spectral response.

Chapter 3, provides brief descriptions of the main experimental setups employed in this thesis: current-voltage (IV), capacitance-voltage (CV), phase-sensitive gain, low temperature and spectral response.

Chapter 4 reports on a study of several alternatives when carrying out the mesa step fabrication process, in order to achieve uniform avalanche gain across a given sample.

Chapter 5 summarises data taken from $Al_{1-x}Ga_xAs_{0.56}Sb_{0.44}$ (x = 0, 0.05, 0.1, 0.15) p^+i^+n diode structures. It is included all results obtained for I-V, C-V, avalanche gain, spectral response, and temperature dependence of avalanche breakdown.

Finally, in Chapter 6 provides a summary for the work carried out along suggestions for future research.

2. Background theory

2.1 APD structures: p+-i-n+ and SAM APD

As indicated in Chapter 1, avalanche photodiodes (APDs) are a type of photodetector that employs the avalanche effect to achieve an internal gain current. This means that APDs are the best choice where amplification of the input signal proves necessary. The most basic APD structure is shown in Figure 1.

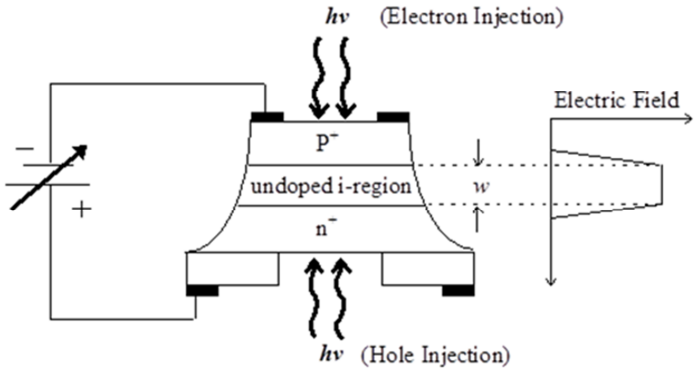

Figure 1 Schematic diagram of a *p+-i-n+* photodiode at reverse bias. On the right, the corresponding electric field is shown.

On the right-hand side, Figure 1 shows the electric field applied across the device when a reverse bias is employed. As soon as the device is illuminated, electron-hole pairs are created in the p+ and n+ cladding layer. These pairs are then accelerated and injected in to the i-region. If the electric field in the i-region is sufficiently high, the carriers become hot and when they collide with lattice atoms, a new electron-hole pair is generated. This mechanism is called avalanche multiplication effect.

A design problem of p-i-n diodes comes to light where high sensitivity is required. As the same layer is used for multiplication and photon absorption, to increase sensitivity, a narrow band-gap material must be employed in the i-region. However, decreasing the band gap entails an increase of the tunnelling current. This trade-off can be avoided using a Separate-Absorption-Multiplication (SAM) APD (see Figure 2).

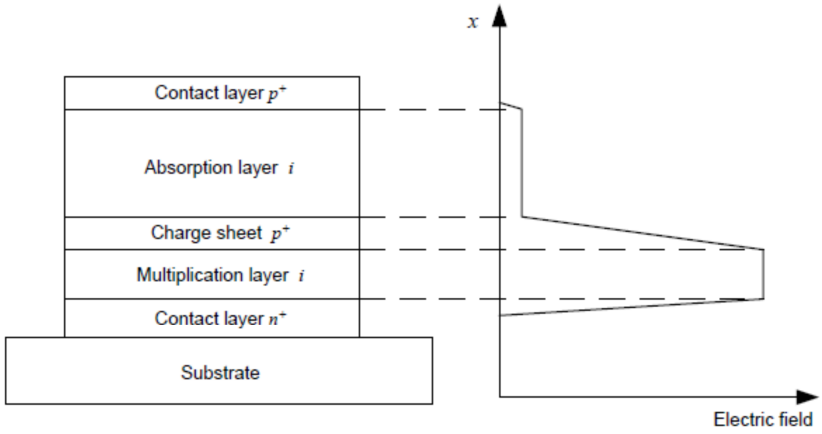

Figure 2 Basic structure of a SAM APD and its electric field at reverse bias

In this new scheme, the absorption and multiplication layers are structurally separated. Therefore, in a SAM APD, current is generated in the absorption layer and the avalanche mechanism takes place in the multiplication layer. The absorption layer is usually made of a narrow band-gap material, to increase photon efficiency. On the other hand, because of its high electric field, the multiplication layer uses a wide band-gap material to decrease tunnelling current. The charge sheet layer is set between these two layers to enable their electric field difference to be controlled. Under these conditions, the absorption layer is fully depleted and its electric field is maintained at a sufficiently low level to enable it to avoid the tunnelling current.

2.2 Avalanche multiplication. Local model

In Figure 3, a schematic diagram is presented for an electron initiated ionisation event. An electron high up in the conduction band (1) loses a portion of its energy (1') to promote a second electron from the valence band (2) to the conduction band (2'). When, the second electron is promoted, it leaves behind a hole. In this manner, an electron-hole pair is created. The same process can be performed if the ionisation event is initiated by a hole, rather than an electron, and the previous explanation serves once each instance of "electron" and "hole" are interchanged.

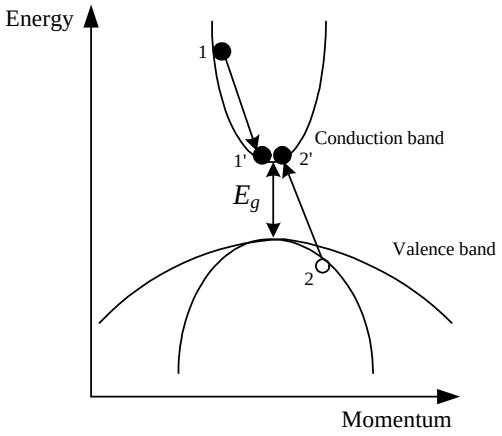

Figure 3 Energy-momentum diagram for an electron initiated ionisation event

Avalanche gain is described by means of the impact ionisation coefficients, α for electron and β for holes. Both are defined as the number of new successful impact ionisation events initiated by a single carrier per unit length travelled, under a given electric field. The inverse of these values represents the average distance that an electron or hole travels along the electric field before an impact ionisation event occurs.

The "local model" is a classic method of describing the impact ionisation mechanism. Here, the impact ionization coefficient can be expressed in terms of the local electric field applied. Both coefficients have been mathematically described by the following expressions: [14,15]

$$\boldsymbol{\alpha(E) = A_1 exp[-\left(\frac{B_1}{E}\right)^{l_1}]} \quad (2.1)$$

$$\boldsymbol{\beta(E) = A_2 exp[-\left(\frac{B_2}{E}\right)^{l_2}]} \quad (2.2)$$

where $A_{1,2}$, $B_{1,2}$, $l_{1,2}$ are constant parameters that are unique for each material and E is the local electric field. As these expressions indicate, the higher the electric field

the larger the ionisation coefficient giving rise to more impact ionisation per unit length.

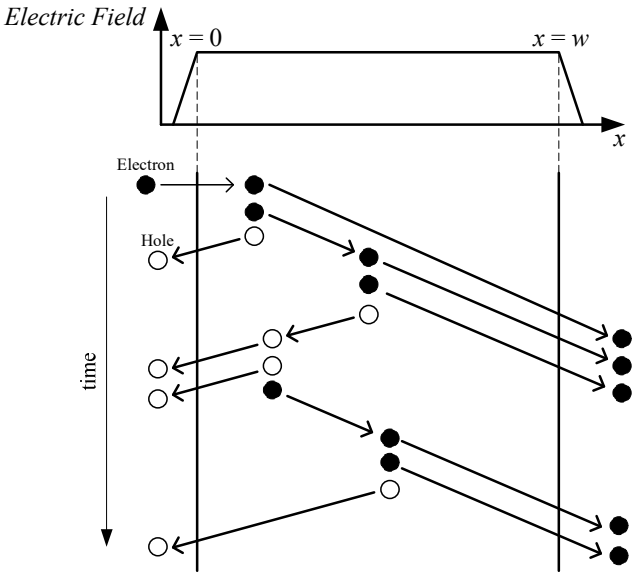

Figure 4 Schematic representation of an electron initiated avalanche multiplication process in a p+-i-n+ diode

A schematic representation of an electron initiated avalanche multiplication process in a p+-i+n+ diode is presented in Figure 4. The *x* and *y* axis represent the position and time, respectively. When an electron is injected into the i-region, it is accelerated by the high electric field applied. Along the path travelled by the electron, *dx*, it will undergo an average αdx of ionising collisions. Where a collision occurs, an electro-hole pair will be created. These newly carriers will also be swept along in the electric field and will undergo αdx collisions before leaving the i-region. The electrons generated close to the right-hand side of the avalanche region will initiate less ionisation events than those created on the left-hand side, as electrons travel in a left to right direction. Via this cascading effect, an injected electron will create a number of new carriers (electrons and holes), giving rise to an average gain *M(x)*. This average gain, based on local model theory, can be written as follows[1]:

$$M(x) = \frac{exp\left[-\int_0^x (\alpha(x\prime)-\beta(x\prime))dx\prime\right]}{1-\int_0^w \alpha(x\prime)\exp\left[-\int_0^x (\alpha(x\prime\prime)-\beta(x\prime\prime))dx\prime\prime\right]dx\prime} \quad (2.3)$$

Where only electrons are injected to initiate the impact ionisation event (x=0), the equation (2.3) can be expressed as follows:

$$M_e = \frac{1}{1-\int_0^w \alpha(x)\exp\left[-\int_0^x (\alpha(x')-\beta(x\prime))dx\prime\right]dx} \quad (2.4)$$

On the other hand, where only holes are injected to initiate the impact ionisation event (x=w), the (2.3) equation takes the following form:

$$M_h = \frac{\exp\left[-\int_0^w [(\alpha(x)-\beta(x)]dx\right]}{1-\int_0^w \alpha(x)\exp\left[-\int_0^x (\alpha(x')-\beta(x\prime))dx\prime\right]dx} \quad (2.5)$$

A useful approximation to simplify (2.3), (2.4) and (2.5) is to assume that the electric field is constant across the i-region. In this case, α and β ionisation coefficients remain independent to the position between x=0 and x=w. Thus, the initial equations, (2.3), (2.4) and (2.5), can be simplified as follows:

$$M_e = \frac{1}{1-\frac{\alpha}{\beta-\alpha}[\exp(\beta-\alpha)w-1]} \quad (2.6)$$

$$M_h = \frac{1}{1-\frac{\beta}{\alpha-\beta}[\exp(\alpha-\beta)w-1]} \quad (2.7)$$

$$M(x) = \frac{\exp[(\beta-\alpha)x]}{1-\frac{\alpha}{\beta-\alpha}[1-\exp(\beta-\alpha)w]} \quad (2.7a)$$

Where $\alpha>>\beta$, the equation (2.6) shows that the highest gain is obtained via a pure injection of electrons. In contrast, where $\beta>>\alpha$, the equation (2.7) shows that the highest gain is obtained via a pure injection of holes.

Another approximation is to consider that α is equal to β. In this case, the equations, (2.6), (2.7) and (2.7a), can be expressed as follows:

$$M = M_e = M_h = \frac{1}{1-\alpha w} \qquad (2.7b)$$

In materials such as AlAsSb [16], or $Ga_{0.52}In_{0.48}P$ [17], $\alpha \sim \beta$ and the equation, (2.7b), can be used to obtain an estimation of the ionisation coefficient.

2.3 Temperature dependence of APDs

The study of the temperature dependence of APDs is of vital importance. It affords useful information on a number of important parameters that describe the performance of the APD. By way of example, I-V temperature dependence enables us to determine the existence of bulk or surface-leakage current domination mechanisms. Furthermore, the relationship between breakdown voltage and temperature can be ascertained, which provides important information to enable us to determine whether an APD proves suitable for a given application.

In the local model, impact ionisation coefficients are dependent on the local electric field. It has been proved that both, α and β coefficients, are temperature dependent. As a result, the break down voltage of the avalanche photodiode is also temperature dependent. This is linked to optical phonon generation and the absorption of the hot carrier population [18]. As soon as the temperature is increased, the phonon scattering rate also rises. Therefore, for a given bias voltage, each carrier loses more energy in the form of phonon emission, resulting in a decrease of the hot carrier population. Consequently, more voltage must be applied to achieve the avalanche effect. That is to say, breakdown voltage is increased in parallel with temperature rises. Figure 5 illustrates the typical temperature dependence of the avalanche multiplication of an APD.

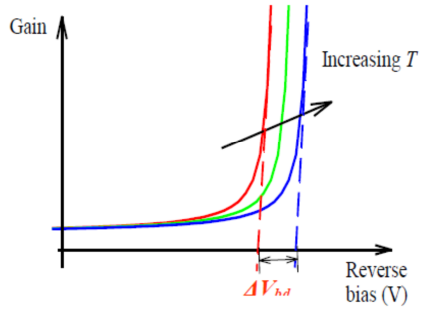

Figure 5 Typical temperature dependence of the avalanche multiplication of an APD

As a general concept, the temperature coefficient of the breakdown voltage, C_{bd}, can be defined as the ratio between the break down voltage variation and the temperature interval:

$$C_{bd} = \frac{\Delta V_{bd}}{\Delta T} \tag{2.8}$$

Expression (2.8) can be used only where there is a linear trend between breakdown voltage and temperature. APDs do not universally demonstrate this behaviour in all temperature ranges; however, most of them evidence a clear linear trend for temperatures ranging between 50K and room temperature [19,20,21].

As indicated above, IV temperature dependence can provide information on bulk or surface-leakage current domination mechanisms. This information can be extracted from the activation energy, E_a, by means of the Arrhenius equation. This equation is expressed as follows:

$$A = A_0 exp\left[\frac{-E_a}{k_b T}\right] \tag{2.8a}$$

where T is the temperature, k_b is the Boltzmann's constant and A and A_0 are constants.

2.4 Excess noise in APDs

The random nature of the impact ionisation process means that the multiplication gain starts to fluctuate around its mean square <*M*>. That is to say, if one carrier is injected into an avalanche region, the resulting gain will have a spread number of values. It is important to note that in the previous section the gain, *M*, has been considered as a unique value. Henceforth, it must be considered as an average value, <*M*>, obtained from a multiple number of values.

This random fluctuation is associated with noise that can be treated as excess noise, independent of traditional shot noise. It can be characterised via the introduction of the excess noise factor, which is defined as the ratio between total noise and the multiplied shot noise. The multiplied shot noise per unit bandwidth, *NiBF*, with a mean multiplication <*M*>, is described as follows [1]:

$$N_{iBF} = 2eI_{pr} < M >^2 \tag{2.9}$$

where *e* is the electron charge and I_{pr} is the primary injected current. Therefore, excess noise, *F*, is calculated as follows:

$$F = \frac{2eI_{pr}<M>^2+\emptyset}{2eI_{pr}<M>^2} \tag{2.10}$$

where ø is the mean square noise generated in the multiplication process. This last term can be expressed as follows:

$$\emptyset = 2eI_{pr}(< M^2 > - < M >^2) \tag{2.11}$$

Thus, *F* can be finally be written in the following manner:

$$F = \frac{<M^2>}{<M>^2} \tag{2.12}$$

Where the random nature of the multiplication is eliminated, the value obtained from (2.12) will be 1. Therefore, in general, we can expect excess noise, *F*, to be higher than unity, and that it will increase as gain rises.

When McIntyre's local model is used to describe the avalanche process, the excess noise factor, *F*, for an electron initiated situation can be expressed in terms of the ratio $k = \beta/\alpha$ [1]:

$$F = kM + (2 - \frac{1}{M})(1 - k) \qquad (2.13)$$

Equation (2.13) shows two basic conditions within APD design to decrease the excess noise. One method entails allowing the carrier with the larger ionisation coefficient to initialise the avalanche process. The second method involves achieving the smallest possible *k* value. When electrons are the injected carriers and $\alpha/\beta = \infty$, equation (2.13) becomes $F = (2 - 1/M)$, which is the lowest achievable excess noise. In contrast, maximum excess noise, $F=\langle M \rangle$, is achieved where electrons remain the injected carriers, but $\alpha=\beta$. Figure 6 shows a graphic representation, obtained from (2.13), of the excess noise factor vs the electron mean multiplication for various values of ionisation coefficient ratios, $k=\beta/\alpha$.

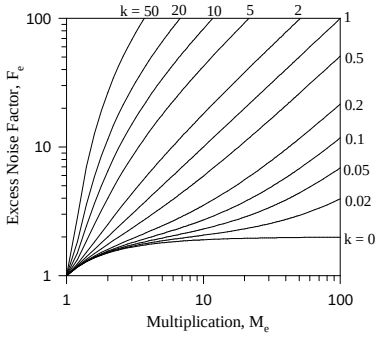

Figure 6 McIntyre's predictions for excess noise factor vs electron mean multiplication for various values of ionisation coefficient ratios $k=\beta/\alpha$

2.5 Non-local random path length model (RPL)

Where the thickness of the multiplication region becomes highly reduced, the local model starts to show its limitations. Therefore, a new non-local Random Path Model (RPL) [22] is employed to predict α and β where the avalanche region becomes excessively thin. RPL is grounded on the concept of dead space d_e (d_h), which is defined as the minimum distance than an electron (hole) has to travel before undergoing impact ionisation. Thus, the path of an electron or hole traveling in the multiplication region can be described by the following probability distribution function:

$$P_e(x_e) = \begin{cases} 0, & x_e < d_e \\ \alpha^* \exp[-\alpha^*(x_e - d_e)], & x_e \geq d_e \end{cases} \tag{2.14}$$

where x_e is the carrier position, and α^* is the saturated ionisation coefficient.

A useful approximation of the dead space d_e (d_h) can be defined as follows:

$$d_e = \frac{E_{the}}{qE} \tag{2.15}$$

$$d_h = \frac{E_{thh}}{qE} \tag{2.16}$$

where E is the electric field, q is the electron charge and E_{the} and E_{thh} are the threshold energies for electrons and holes, respectively.

On the basis of (2.15) and (2.16), the relationship between the local and RPL models can be determined as follows:

$$\frac{1}{\alpha} = d_e + \frac{1}{\alpha^*} \tag{2.17}$$

$$\frac{1}{\beta} = d_h + \frac{1}{\beta^*} \tag{2.18}$$

Models that include the dead space effect envisage a substantial reduction in excess noise in comparison with the local model.

2.6 Device bandwidth

Bandwidth is a very important characteristic of APDs, as high data transmission systems require a fast device response. Bandwidth is largely determined by four main factors: the RC factor, transit time, diffusion time and avalanche gain.

R-C limited bandwidth is linked to the series resistance and capacitance inherent to the photodiode, and can be described as follows:

$$B_{RC} = \frac{1}{2\pi R C_j} \tag{2.19}$$

Capacitance, C_j, is dependent upon the depletion width of the p-n junction, whilst series resistance, R, depends mainly on the metallic contact of the device.

Transient time limited bandwidth relates to the time required by the carriers to cross the depletion region. Most APDs are designed to allow carriers to be created in the depletion layer, under an electric field that is sufficiently high to accelerate them to their saturation velocities. It can be expressed as follows[23]:

$$B_{tr} = 0.45 \frac{v_s}{w} \tag{2.20}$$

where w is the depletion layer thickness and v_s is the saturation velocity.

As we can see, a reduction of the *i*-region layer thickness will effectively decrease the carrier's transit time.

Diffusion limited bandwidth is associated with diffusion time. It is defined as the time that the carriers generated in the neutral region require to reach the depletion layer, and can be expressed as follows:

$$\tau_{diff} = \frac{x^2}{2D_c} \tag{2.21}$$

where x is the diffusion distance and D_c is the minority carrier diffusion coefficient. The diffusion time can mathematically defined as follows:

$$B_{diff} = \frac{1}{2\pi\tau_{diff}} = \frac{D_c}{\pi x^2} \tag{2.22}$$

Avalanche gain bandwidth represents the main limitation of an APD. As the gain is increased, more carriers are created in the multiplication region and more time is required for the avalanche process to decay.

The defined gain-bandwidth product is associated with this limiting factor. It determines the dependence between bandwidth and the avalanche gain from high speed APDs. Figure 7 shows a typical APD graph of bandwidth vs avalanche gain.

Many APDs exhibit a sharp increase in bandwidth with avalanche gain, evident in region I. At low gain, where M<5, this is probably due to the slow diffusion time of the carrier in the undepleted absorption region. The electric field in the absorption region has not been optimised, whereby photocarriers are absorbed and slowly diffused into the multiplication region. As the electric field increases, the carriers' velocity quickly builds up, thereby rapidly increasing bandwidth. For well optimised APD structures, where the absorption region is fully depleted at punch voltage, and carrier velocity builds up quickly, increased bandwidth with avalanche gain is not observed.

In region II, the bandwidth is relatively constant for moderate gain values, which might be explained in two manners: first, it might be attributed to the RC limited bandwidth, as an APD has a voltage dependent capacitance and load resistance which is similar to a p-i-n photodiode, whereby contact resistance and device and parasitic capacitances should be minimized to improve the bandwidth; alternately, it might be attributed to transit-time-limited bandwidth. In structures with a long

absorption region and a thin multiplication region, the carriers are drifting through a long absorption layer with a much lower electric field than the multiplication region. To achieve very high bandwidth in region II, the total carrier transit time must be reduced. Consequently a thinner absorption layer should be employed; however, this will lead to an increase in device capacitance. It is a trade-off between quantum efficiency, transit-time-limited bandwidth and RC bandwidth.

In region III, where there is high gain, bandwidth starts to roll off as the avalanche duration (including build up and decay times) starts to dominate. To reduce the avalanche duration time, it is necessary to adopt a very thin avalanche region or a material wherein k = 0.

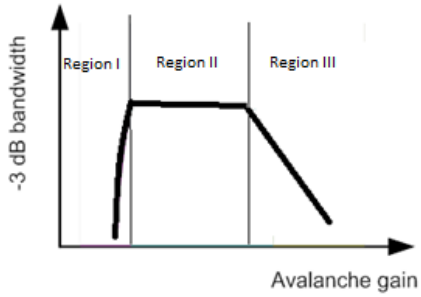

Figure 7 An example of APD bandwidth vs avalanche gain

2.7 Spectral response

Spectral response is defined as the ratio between the current generated by a photo detector and its optical power input. This is associated with the sensitivity that a photo detector evidences as a function of the wavelength of the input signal. The maximum frequency at which the semiconductor has null spectral response is usually referred to as the cut-off wavelength, which is determined by the band gap of the semiconductor, and it can be expressed via the following expression:

$$\lambda_{cutoff} = \frac{hc}{E_g} \tag{2.22a}$$

where h is Planck's constant, c is the light velocity constant an E_g is the band gap of the material.

3. Characterisation techniques

3.1 Current-voltage measurement

On the basis of current-voltage (IV) characteristics, it is possible to obtain an electrical response from the dark current of the APDs. Dark current analysis is an important test for semiconductor devices, as it provides useful information relating to their electrical behaviour. Parameters of interest include the leakage-current components, breakdown voltage or the ideality factor, amongst others. IV measurements for this work were carried out by employing either a HP4140B Pico ammeter or a Keithley 237 source measure unit, under dark conditions.

Forward bias

Careful analysis of the forward bias affords an accurate value of the ideality factor and series resistance, R_s. The ideality factor provides information enabling determination of the dominant current mechanisms flowing through an APD. For its part, series resistance limits the *RC* bandwidth and increases the drop voltage across the device.

When forward bias is applied, the diode model can be expressed as follows[24]:

$$I_F = I_0[exp\left(\frac{q(V-IR_s}{nkT}\right) - 1] \quad (3.1)$$

where q is the electron charge, I_0 is the saturation current, k is Boltzmann's constant, T is the temperature expressed in Kelvin, R_s is the series resistance and n is the ideality factor, which falls between a range of 1 and 2. A factor close to 1 indicates that the dark current is entirely dominated by diffusion. In contrast, values close to 2 shows that the generation-recombination is the dominating mechanism.

At low voltage, the bias caused by series resistance is neglible. However, at high voltages, where *IRs >> V*, series resistance dominates the drop voltage throughout the device and by fitting the IV curve, *Rs* can be determined.

Reverse bias

As indicated in Chapter 2, APDs operate under reverse bias in order to obtain gain from the avalanche effect. Dark current is an important parameter in terms of determining APD performance, as it significantly degrades the signal-to-noise ratio, and it can be lowered, either by enhancing the quality of the epitaxial structure, or by improving manufacturing processes. In this research, dark current measurements were carried out employing devices of different sizes, in order to determine whether dark current is bulk or surface dominant. If the dark current scales well in the perimeter, this indicates that the surface leakage current is dominant due to the conducting paths formed along the device mesa surface.

Another leakage current component that can be observed as a result of the reverse bias is the band-to-band tunnelling current. It becomes important when the applied electric field is of a sufficiently high level, and can be expressed as follows:

$$I_{tunn} = \frac{(2m^*)^{0.5} q^3 EVA}{h^2 E_g^{0.5}} \exp[-\frac{2\pi\sigma_T (m^*)^{0.5} E_g^{1.5}}{qhE}] \quad (3.2)$$

where q is the electron charge, m^* is the effective electron mass, E is the electric field applied, A is the device area, h is Plank's constant, E_g is the band gap and σ_T is a constant that depends on the specific shape of the tunnelling barrier. For any given material, band-to-band tunnelling current imposes a lower limit on avalanche region width.

3.2 Capacitance-voltage measurement

When an AC voltage is applied over a diode, it causes a charge variation within the depleted region. This behaviour is associated with intrinsic capacitance, C_j. The basic theory defines this capacitance, C_j, via the following equation:

$$C_j = \frac{\varepsilon_0 \varepsilon_r A}{d_w} \tag{3.3}$$

where ε_r is the dielectric constant of the material, ε_0 is vacuum permittivity, A is the junction area and d_w is the depletion width.

Poisson's equation defines the gradient of the electric field profile as follows:

$$\frac{dE}{dx} = \frac{qN}{\varepsilon_0 \varepsilon_r} \tag{3.4}$$

where E is the electric field profile, q is the electron charge and N is the activated dopant density.

By employing a capacitance-voltage (CV) measurement technique and calculating equation (3.3) and (3.4) we are able to model the CV profile of any APD. Therefore, the data obtained from this model can be compared with the experimental data to enable us to determine the depletion width thickness and the electric field profile. Refer to the example provided in Figure 8.

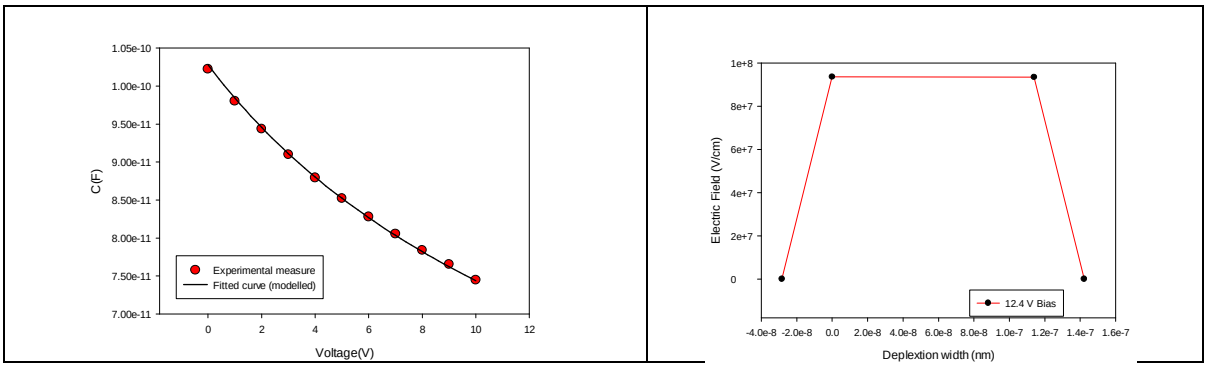

Figure 8 Example of CV curve fitting and the electric field profile obtained

Other important information that can be obtained from CV measurement is the degree of undercut that the devices display due to manufacturing processes. To determine this, devices of different sizes are measured and the results are scaled in area. Where small devices display higher scaled values than larger devices, this indicates that the area has been overestimated in view of their considerable undercut.

All CV measures in this thesis were carried out using a HP4257 LCR meter.

CV profile of a SAM APD

A typical CV response from a SAM APD is outlined in the Figure 9. At lower bias, capacitance decreases gradually until the charge sheet is completely depleted. At this point, capacitance abruptly decreases due to the rapid depletion of the absorption layer. This bias voltage is usually referred to as “punch through”, and in practice it is a key feature that has significant bearing on SAM APD performance.

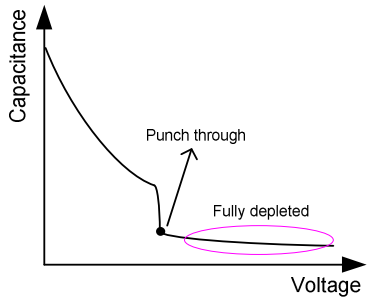

Figure 9 Typical CV response in SAM APDs

3.3 Phase sensitive multiplication measurement

As indicated above, avalanche gain is a key feature of APD performance. A schematic view of the photo-multiplication setup is presented in Figure 10. The laser signal is chopped at a frequency of 180Hz to create an AC photocurrent, $I_{ph,}$ in the device under test (DUT). A source measure unit (SMU) is employed to apply a bias voltage to the DUT. The same induced photocurrent frequency in the DUT is also applied to the resistor situated in series. I_{ph} across the resistance provides an AC

voltage that is measured via a locking-amplifier (LIA). Finally, an external reference from the chopper controller feeds the LIA.

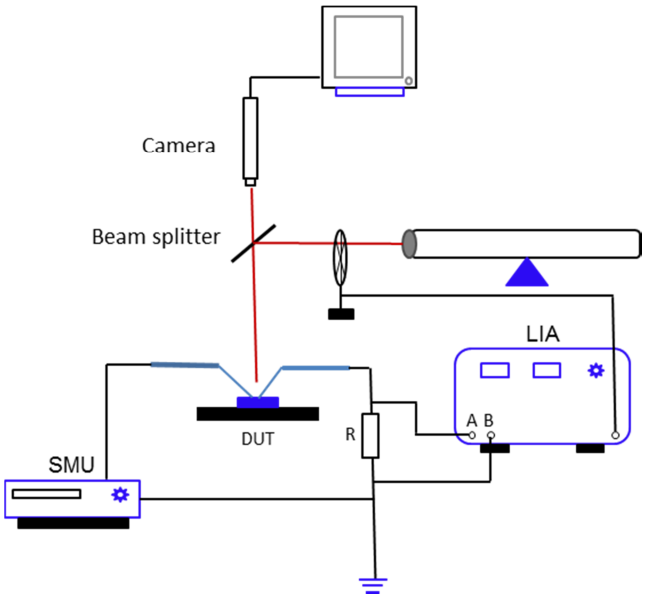

Figure 10 Schematic phase sensitive multiplication setup

LIAs are employed to extract a signal with a determined carrier wave within a high-noise environment via the phase sensitive technique. In this technique, the input signal is multiplied by a reference signal with the same frequency. A schematic of phase sensitive detection is shown in Figure 11.

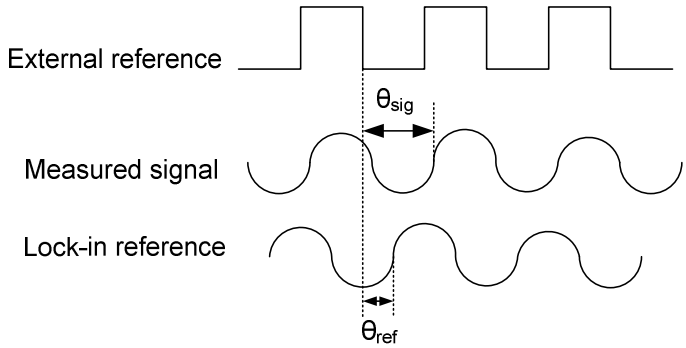

Figure 11 Schematic of the phase detection technique

The mathematical expressions for the measured signal and the lock-in amplifier reference signal are as follows:

$$V_{sig} = A_{sig} \sin(w_{sig}t + \theta_{sig}) \quad (3.5)$$

$$V_{ref} = A_{ref} \sin(w_{ref}t + \theta_{ref}) \quad (3.6)$$

where A_{sig} and A_{ref} are the amplitudes , W_{sig} and W_{ref} are the frequencies and θ_{sig} and θ_{ref} are the phases.

If both equations are multiplied the result is as follows:

$$V_o = V_{sig} \times V_{ref} = A_{sig}A_{ref} \sin(w_{sig}t + \theta_{sig}) \sin(w_{ref}t + \theta_{ref}) \quad (3.7)$$

The expression can be developed as indicated below:

$$V_0 = \frac{1}{2}A_{sig}A_{ref}[\cos(w_{sig}t - w_{ref}t + \theta_{sig} - \theta_{ref}) - \cos(w_{sig}t + w_{ref}t + \theta_{sig} + \theta_{ref})] \quad (3.8)$$

Thus, there are two terms in this expression: the first entails a high frequency component ($w_{sig}t + w_{ref}t$) and the second, a low frequency component ($w_{sig}t - w_{ref}t$). Upon passing this signal through a low-pass filter, the high frequency is filtered out. However, if the LIA forces the reference signal to have the same frequency as the input signal ($w_{sig=}w_{ref}$), the final output will be a DC component:

$$V_0 = \frac{1}{2}A_{sig}A_{ref} \cos(\theta_{sig} - \theta_{ref}) \quad (3.9)$$

Evidently, the measured signal has been isolated from the harmonic components and the output is a proportional value of the input signal amplitude.

The gain measurement is calculated via the ratio between the primary photocurrent and the multiplied photocurrent, as follows:

$$M(V) = \frac{I_{ph}}{I_{pr}} \quad (3.10)$$

where I_{pr} is the primary photocurrent and I_{ph} is the measured photocurrent.

I_{pr} refers to the photocurrent obtained as the APDs depletion width is increased. It has been reported [25] that the primary photocurrent increases linearly with the bias, whilst the cladding layers slowly deplete. Therefore, I_{pr} can be extrapolated from photocurrent values obtained at lower biases, where a multiplication event has yet to take place. An example of a multiplication measurement is provided in Figure 12.

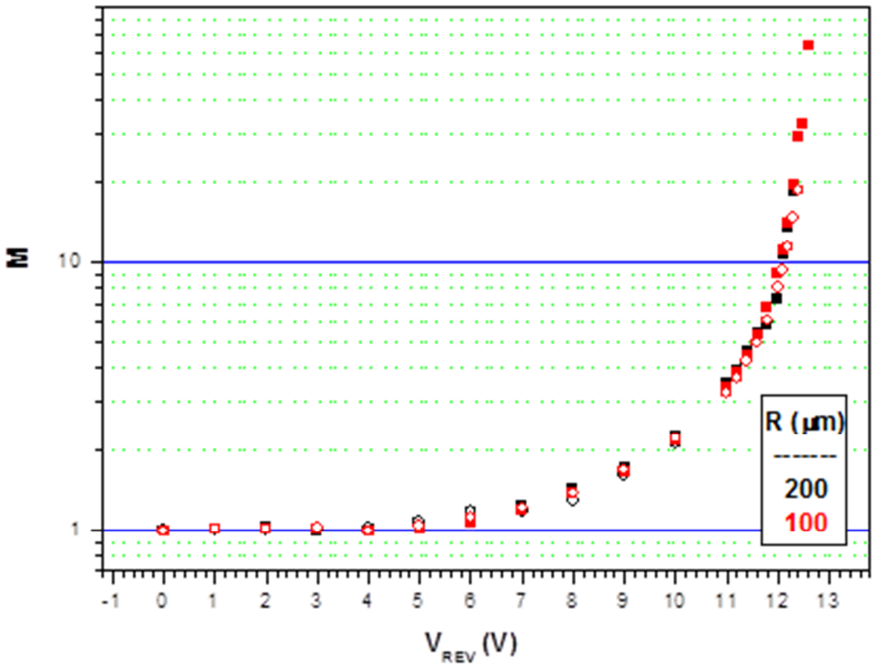

Figure 12 Example of an avalanche multiplication measurement

3.4 Low temperature measurement

As indicated in 2.3, APD low temperature measurement is essential in order to study features that cannot be observed at room temperatures: for instance, dark current mechanisms display different behaviour at low temperatures and at room temperature.

All temperature dependence measurements presented in this thesis were carried out in the Janis ST-500 probe station (refer to Figure 13). The setup consists of two DC

probe arms and a multimode fibre that can be paired to any optical source, from visible light to near infrared. The chamber can be pumped down to a vacuum of $<2e10^{-5}$ mbar and cooled down by an open circuit of nitrogen. Sample temperatures can fall within a range spanning between 77K and room temperature.

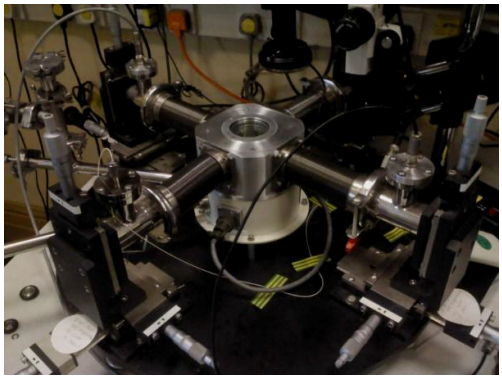

Figure 13 Janis ST-500 probe station setup

3.5 Monochromator set-up

As indicated in section 2.7, for a given semiconductor, the cut-off wavelength of the spectral response will vary in accordance with its band-gap. Figure 14 presents various spectral responses from a number of semiconductors.

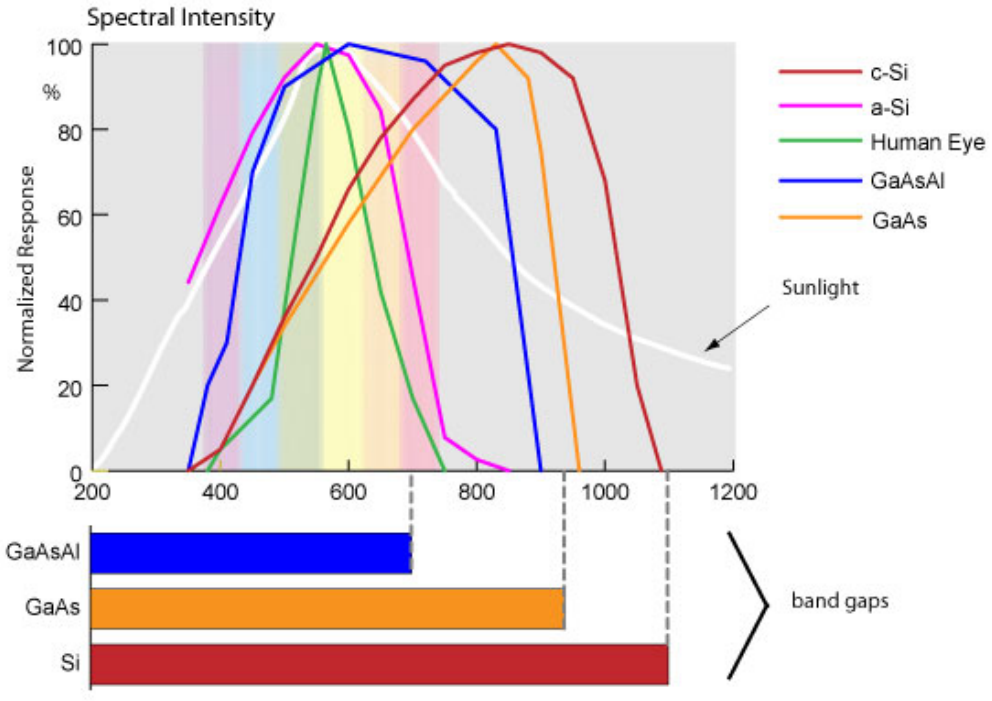

Figure 14 Normalized spectral response from several semiconductors

The set-up employed to measure spectral response within this research is mainly based on the use of a monochromator, a piece of optical equipment that allows a selectable narrow band of light to be mechanically split and transmitted from a wider band source. Figure 15 presents the set-up used. A lamp (usually a tungsten lamp) is employed as a wide band source. It is focused directly on to the input of the monochromator. The monochromator boasts two customised split outputs to measure devices, each with a focal length of 340 mm, and can be adjusted to cover different wavelength intervals (400nm, 1um and 2um). Focusing lenses are installed at each output to collect the optic signal, and low-pass filters are used to remove high order signals. To avoid noisy measurements, where a device displays high leakage current, a phase-sensitive detection (PSD) structure (refer to section 3.3) was employed. This includes a chopper situated after each output, a SMU for biasing the devices, a LIA and a bias resistor, R. When taking measurements, a commercial photodiode with a predictable spectral response is normally employed at one of the monochromator outputs. This enables calibration of the power distribution of each wavelength within the system whilst the DUT is being measured. After the measurement has been carried out, the raw data obtained from the DUT is corrected and normalised on the basis of this distribution.

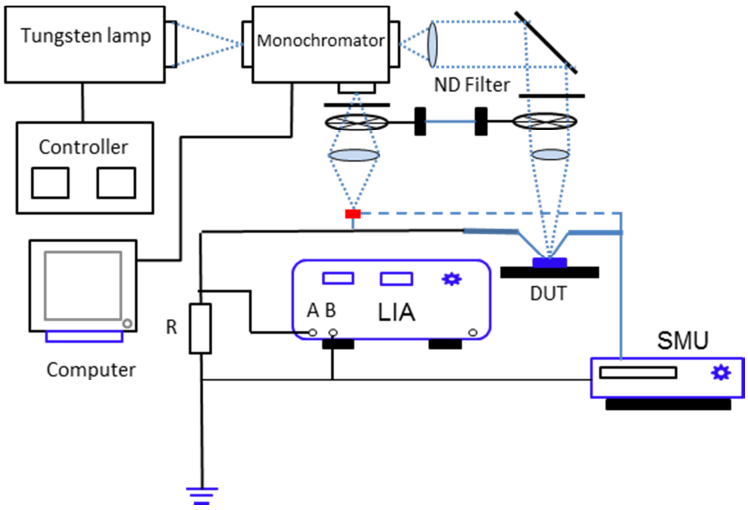

Figure 15 Scheme of the Monochromator set-up

4. InGaAs/AlAsSb SAM APD. Wet etch study.

4.1 Introduction

Premature edge breakdown is of critical importance for the optimal DC performance of SAM APD devices. Table 1 presents an example structure of an AlAsSb SAM APD. In Figure 16 can be seeing that premature edge breakdown stems from the severe undercut on the mesa sidewall, while the AlAsSb avalanche layer is being etched during mesa formation. Standard mesa etching procedure based on H_2SO_4:H_2O_2:H_2O and HCl:H_2O_2:H_2O mixtures for the selective etching of InGaAs and AlAsSb, respectively [16,26], shows that premature edge breakdown is yet to be resolved. The undesirable shape of this side wall region is characterised by localised regions, also referred to as 'hot-spots', that possess a high electric field [27]. As impact ionisation is triggered by high electric fields, the current flowing along the device edge is very high, adversely affecting DC performance (tunnelling) and eventually leading to premature degradation. This issue is of particular importance in devices designed for high-speed applications, due to their small dimensions. In order to address the issue of premature breakdown, the following options are available:

(A) Determining the best combination of wet etchants that will etch the mesa and supress the severe undercut.
(B) Studying dry etching as an alternative.

Doping type	Material	Doping density		Thickness	
		Nominal (cm^{-3})	Fitted (cm^{-3})	Nominal (nm)	Fitted (nm)
p^+ contact	InGaAs	1×10^{19}	-	10	-
p^+ cladding	InAlAs	$>5\times10^{18}$	5×10^{18}	300	-
i grading	InAlGaAs (Eg ~ 1.1 eV)	$<2\times10^{15}$	1×10^{15}	50	50
i absorption	InGaAs	$<2\times10^{15}$	6×10^{15}	500	500
i grading	InAlGaAs (Eg ~ 1.1 eV)	$<2\times10^{15}$	2×10^{16}	50	50
p charge sheet	InAlAs	5×10^{17}	2.9×10^{17}	55	55
i intrinsic	InAlAs	$<2\times10^{15}$	1×10^{16}	50	50
p charge sheet	AlAsSb	1×10^{18}	4×10^{17}	44	44
i multiplication	AlAsSb	$<2\times10^{15}$	1×10^{16}	50	40
n^+ cladding	AlAsSb	$>5\times10^{18}$	5×10^{18}	100	-
n^+ contact	InGaAs	1×10^{19}	-	300	-
Semi-insulating InP					

Table 1 Structure of an AlAsSb SAM APD 1 (REV2)

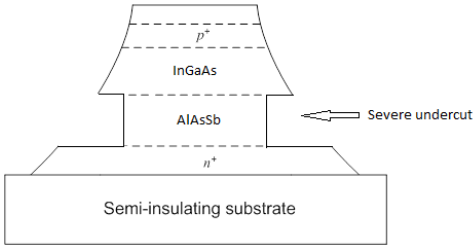

Figure 16 Cross-section scheme of a SAM APD InGaAs/AlAsSb with severe undercut

4.2 Wet etching study

SAM APD 1(REV 2) (refer to Appendix I) was the InGaAs/AlAsSb SAM APD structure sample employed to carry out this research.

To date, the wet etchants that have been employed to etch the mesa structure of SAM APD devices are H_2SO_4:H_2O_2:H_2O (1:8:80) and HCL:H_2O_2:H_2O (1:1:5) (refer to Appendix 2). The duration of the etching was empirically determined via the change in the colour of the sample surface during the wet etching procedure. H_2SO_4:H_2O_2:H_2O (1:8:80) was employed to etch the InGaAs/InAlAs/InAlGaAs layers, HCL:H_2O_2:H_2O (1:1:5), to etch the AlAsSb layer, and finally H_2SO_4:H_2O_2:H_2O (1:8:80) was used to partially etch the bottom n+ contact InGaAs layer. The change in the sample surface colour from green to black and then back to green is indicative of the sequence in which the aforementioned wet etchants were employed. The black regions that formed on the AlAsSb layer are oxidized areas.

With a view to resolving the issue of premature breakdown voltage, three sets of trials were carried out.

4.2.1 Standard wet etch review

The first set of trials focused on standardising the duration of the etching of the aforementioned wet etchants. Amongst the trials conducted, the combination that afforded the lowest AlAsSb oxidation expansion on the device surface was a two-

step etching procedure involving H_2SO_4:H_2O_2:H_2O (1:8:80) for 3 minutes followed by HCL:H_2O_2:H_2O (1:1:5) for 9 seconds. A third etching step proved unnecessary (although it was initially held to be requisite). The mesa structure was etched down to almost the halfway point of the n+ contact InGaAs layer. It was assumed that HCL:H_2O_2:H_2O (1:1:5) would have acted as a selective etchant of the InGaAs layer and it was expected that it would not etch the bottom n+ contact InGaAs layer. This sample was further DC characterised. The IV diagrams show that the leakage current scales with the perimeter (surface dominated dark current) and also the area (bulk dominated dark current). The tunnelling current can probably be ascribed to the low band-gap (InGaAs) absorption layer.

Figure 17 to Figure 25 present the I-V and C-V measurements taken from SAM APD 1 (REV 2) subsequent to etching in H2SO4:H2O2:H2O (1:8:80) for 3’ and HCL:H2O2:H2O (1:1:5) for 9’’, whilst Figure 26 includes a number of SEM images of the cross-section of a device side-wall.

It is worth noting that we did not extract the electric field profile from CV measurements. Therefore, we are unable to determine whether or not the other layers (i.e. multiplication) contribute to the tunnelling mechanism due to high electric field values. Furthermore, no temperature dependent IV measurements were obtained, in order to ascertain whether or not the tunnelling mechanism is sensitive (trap-assisted tunnelling) or insensitive (direct tunnelling) to temperature. In accordance with the CV measurements, the punch-through voltage (where the entire device is depleted) was recorded as 8V.

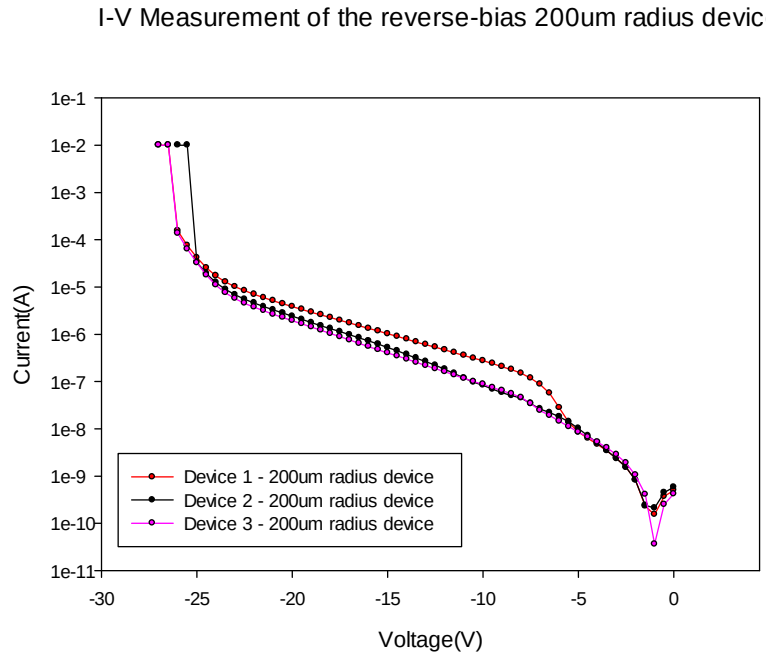

Figure 17 Reverse I-V from SAM APD 1 (REV 2) subsequent to etching in H2SO4:H2O2:H2O (1:8:80) for 3' and HCL:H2O2:H2O (1:1:5) for 9'' (Standard recipe). 200um radius device.

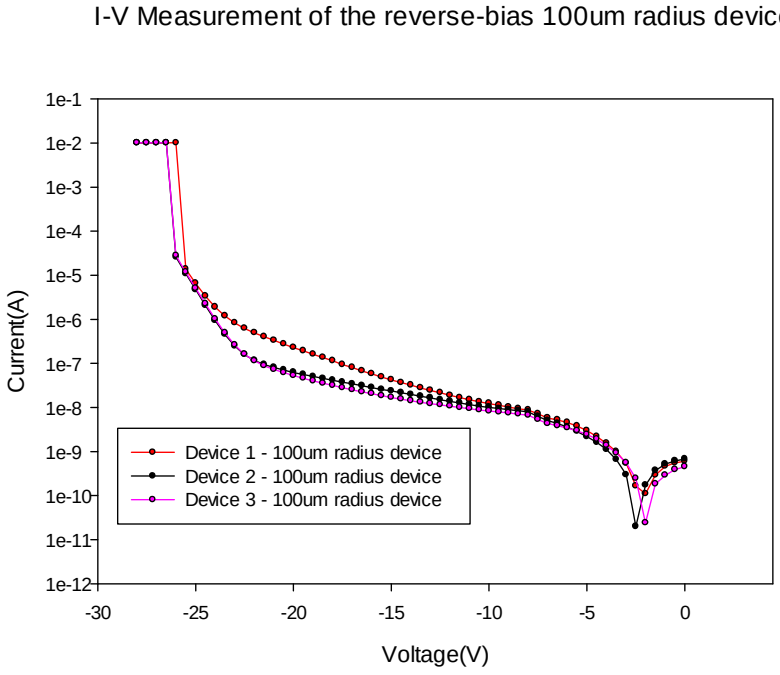

Figure 18 Reverse I-V from SAM APD 1 (REV 2) after etch in H2SO4:H2O2:H2O (1:8:80) for 3' and HCL:H2O2:H2O (1:1:5) for 9'' (Standard recipe). 100um radius device

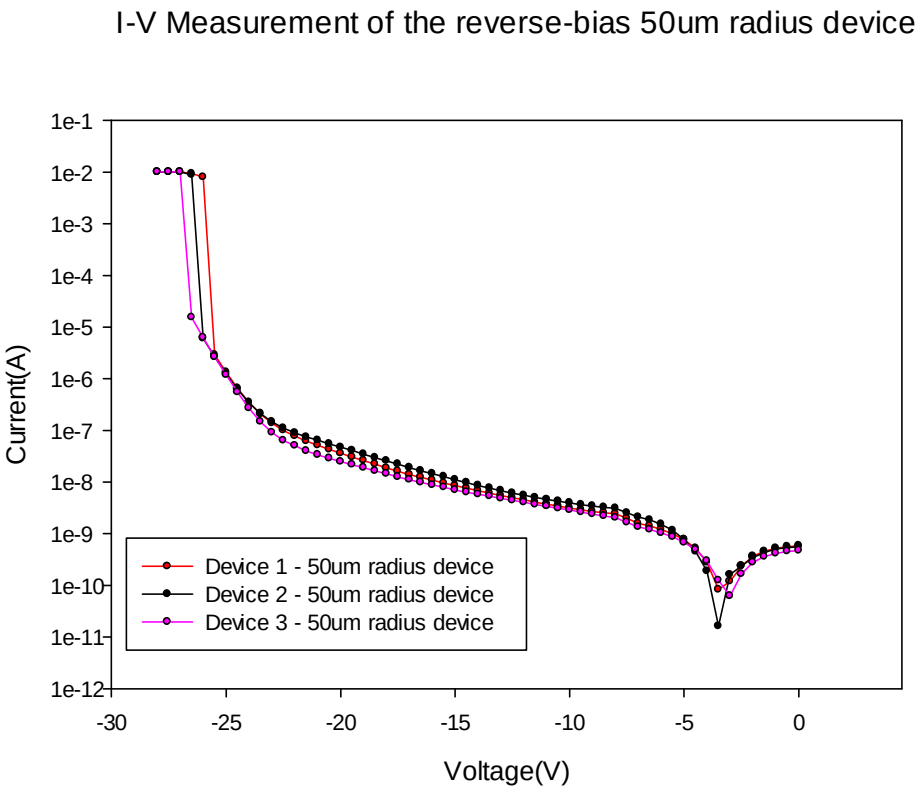

Figure 19 Reverse I-V from SAM APD 1 (REV 2) subsequent to etching in H2SO4:H2O2:H2O (1:8:80) for 3' and HCL:H2O2:H2O (1:1:5) for 9'' (Standard recipe). 50um radius device.

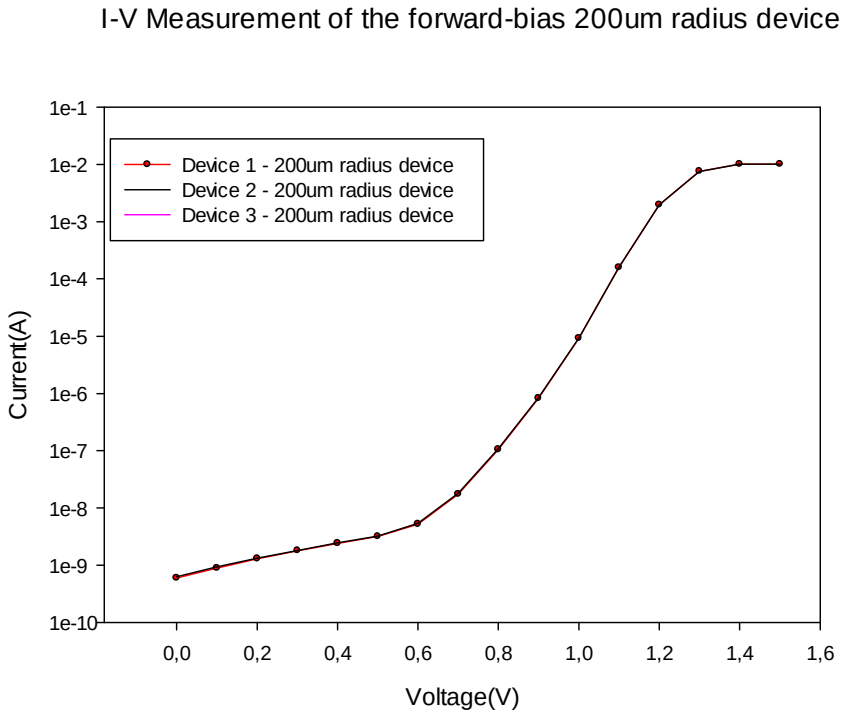

Figure 20 Forward I-V from SAM APD 1 (REV 2) subsequent to etching in H2SO4:H2O2:H2O (1:8:80) for 3' and HCL:H2O2:H2O (1:1:5) for 9'' (Standard recipe). 200um radius device

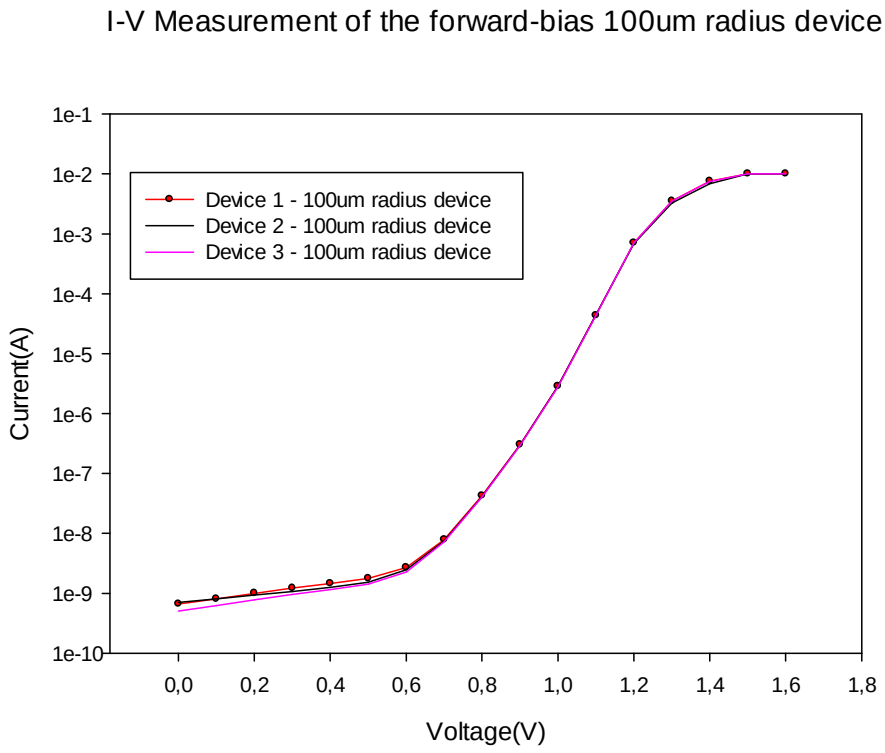

Figure 21 Forward I-V from SAM APD 1 (REV 2) subsequent to etching in H2SO4:H2O2:H2O (1:8:80) for 3' and HCL:H2O2:H2O (1:1:5) for 9'' (Standard recipe). 100um radius device

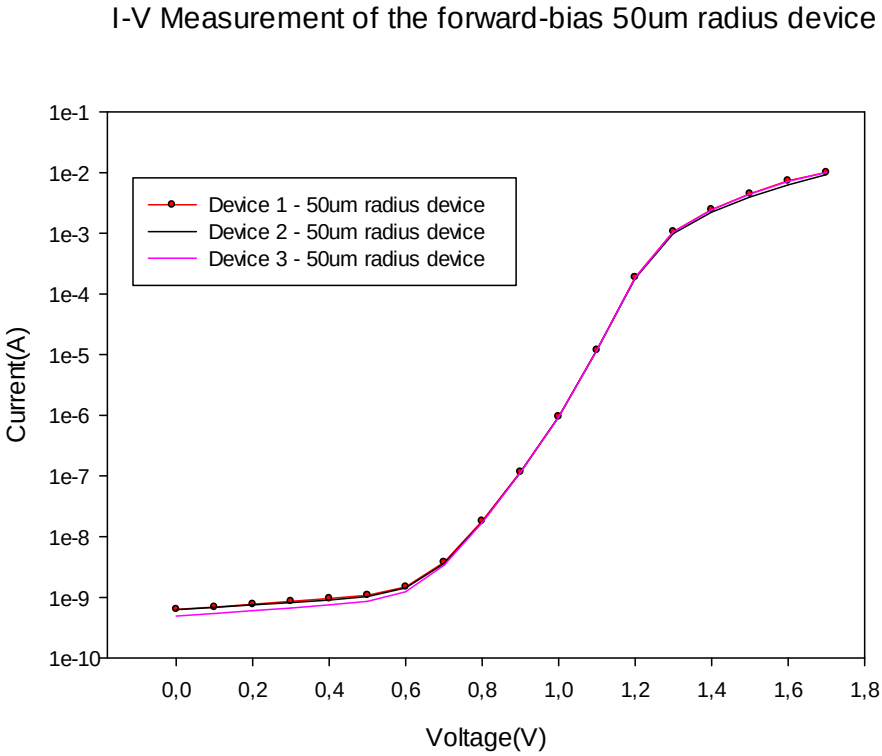

Figure 22 Forward I-V from SAM APD 1 (REV 2) subsequent to etching in H2SO4:H2O2:H2O (1:8:80) for 3' and HCL:H2O2:H2O (1:1:5) for 9'' (Standard recipe). 50um radius device

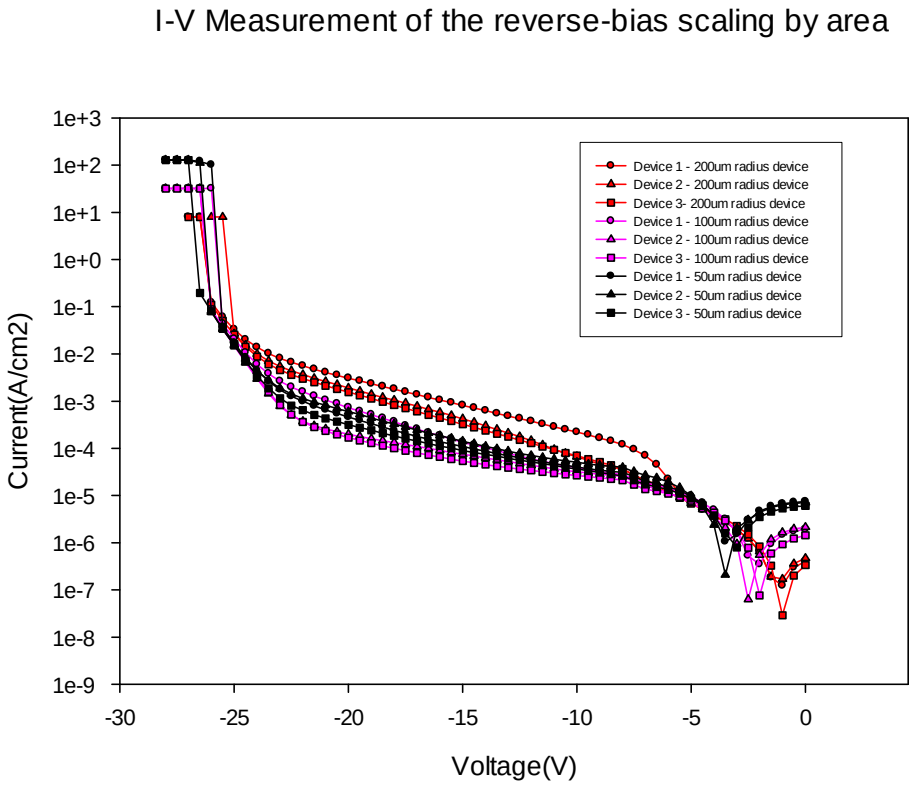

Figure 23 Reverse I-V from SAM APD 1 (REV 2) subsequent to etching in H2SO4:H2O2:H2O (1:8:80) for 3' and HCL:H2O2:H2O (1:1:5) for 9'' (Standard recipe). It has been scaled in area for 200um, 100um and 50um radius device.

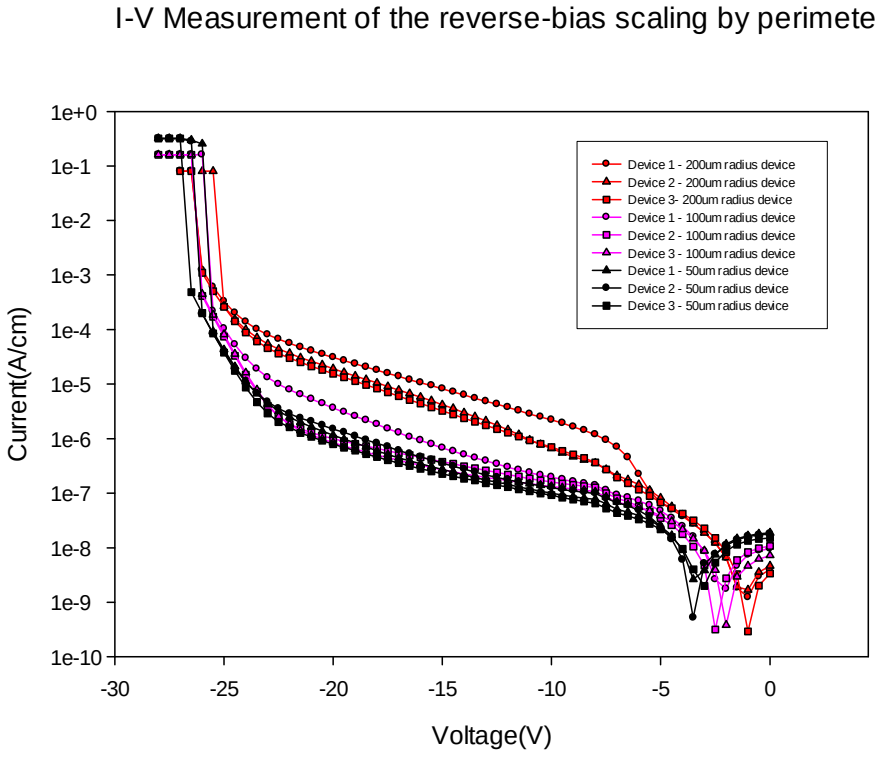

Figure 24 Reverse I-V from SAM APD 1 (REV 2) subsequent to etching in H2SO4:H2O2:H2O (1:8:80) for 3' and HCL:H2O2:H2O (1:1:5) for 9'' (Standard recipe). The perimeter has been scaled for 200um, 100um and 50um radius devices.

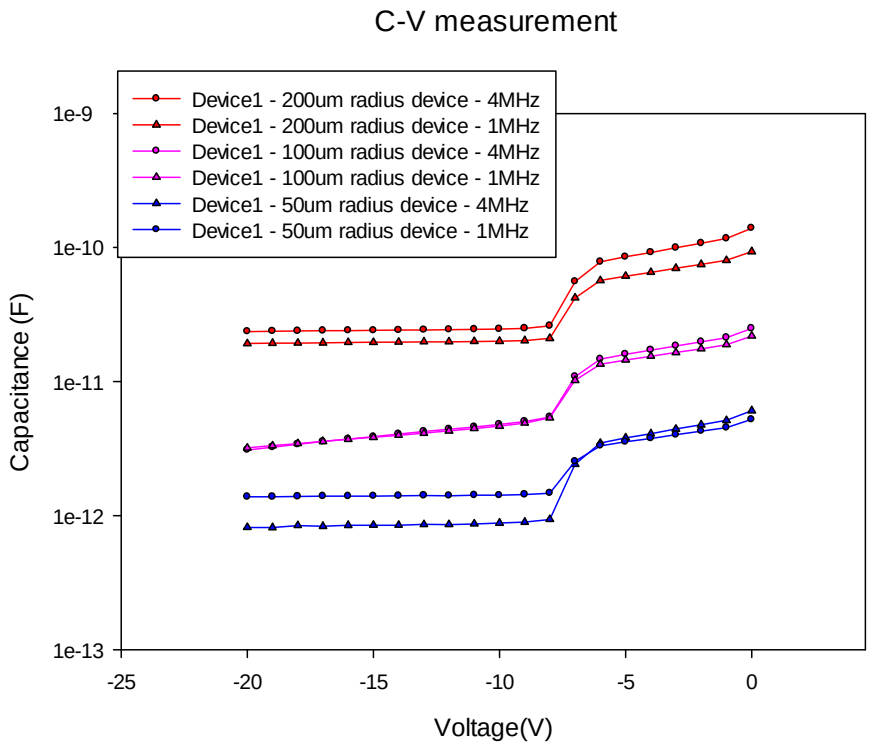

Figure 25 C-V measurement from SAM APD 1 (REV 2) subsequent to etching in H2SO4:H2O2:H2O (1:8:80) for 3' and HCL:H2O2:H2O (1:1:5) for 9'' (Standard recipe), for 200um, 100um and 50um radius devices and for 4MHz and 1MHz frequency measure signals.

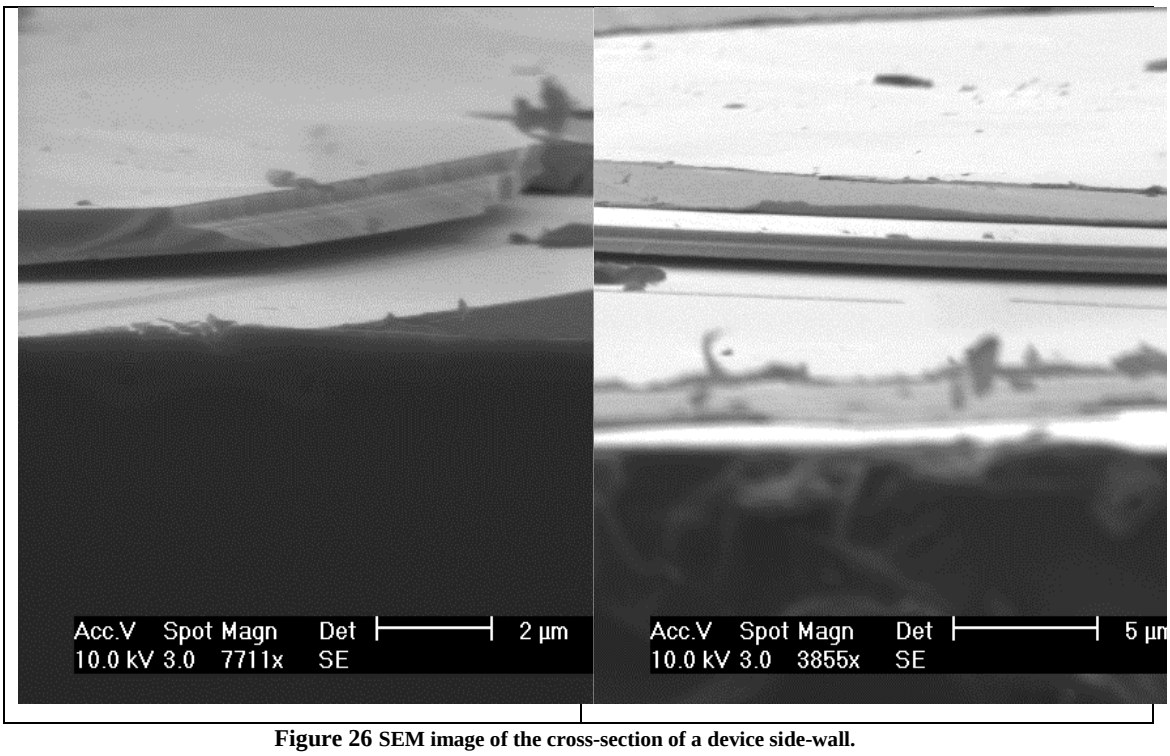

Figure 26 SEM image of the cross-section of a device side-wall.

The following additional trials were performed with a three-step etching procedure:

1) H_2SO_4:H_2O_2:H_2O (1:8:80), HCL:H_2O_2:H_2O (1:1:5), H_2SO_4:H_2O_2:H_2O (1:8:80), which proved entirely unsuccessful.

2) H_2SO_4:H_2O_2:H_2O (1:8:80), HCL:H_2O_2:H_2O (1:1:5), HBR:CHECOOH:$K_2CR_2O_3$ (1:1:1) did not afford any promising results, particularly in terms of the BR:CHECOOH:$K_2CR_2O_3$ (1:1:1) step, where etching times of 1sec and 10sec over-etched the mesa structures and eventually led the respective APD devices to behave as if they were “open-circuited”.

4.2.2 Wet etch trials

The second set of trials involved testing different wet etchants than those employed in (i). The trials did not lead to successful results as the etchants were either non-selective, and mesa structures were eventually over-etched, or proved inert (the mesa structures remained unetched). Below, a list of the etchants employed is provided. These trials entailed one-step etching procedures, wherein each individual etchant was used only for a single sample (as opposed to combinations of etchants).

- HBr: HNO_3:H_2O (1:1:30) (non-etching)
- HBr: HNO_3:H_2O (1:1:10) (non-etching)
- NH_4:H_2O_2:H_2O (1:1:100) (non-etching)
- H_3PO_4: H_2O_2:H_2O (3:1:50) (over-etching)
- H_3PO_4: H_2O_2:H_2O (3:4:5) (over-etching)
- H_3PO_4: H_2O_2:H_2O (3:4:15) (over-etching)
- H_2SO_4: HCL: H_2O_2 (1:1:8) (over-etching)
- H_2SO_4: HCL: H_2O_2 (1:1:16) (over-etching)
- H_2SO_4:H_2O_2:H_2O (1:8:30) (over-etching)

4.2.3 Diluted HCl:H_2O_2:H_2O etchant

The third set of trials entailed a two-step etching procedure, initially employing H_2SO_4:H_2O_2:H_2O (1:8:80) as an etchant, and subsequently diluted HCL: H_2O_2:H_2O. The trials were as follows:

1) H_2SO_4:H_2O_2:H_2O (1:8:80) for 3 minutes and HCL: H_2O_2:H_2O (1:1:60) for 26 minutes (4-min steps). This etching process caused the mesa structure to become over-etched. The devices were further processed and DC tested, and behaved as if they were “open-circuited”.

2) H_2SO_4:H_2O_2:H_2O (1:8:80) for 3 minutes, HCL:H_2O_2:H_2O (1:1:5) for 5 seconds and HCL:H_2O_2:H_2O (1:1:60) for 2 minutes. Following further processing and DC testing of the manufactured devices, only a small number proved operational. Most of them behaved as if they were “open-circuited”. The device breakdown voltage was recorded as 22-24V.

5. AlGaAsSb PIN diodes

5.1 Introduction

Reported I-V measurements from AlAsSb PIN diodes [14] indicate a significantly high surface-leakage current. Al and Sb atoms are prone to form oxide compounds due to chemical reactions with oxygen-based etchants or with air [28]. The idea of incorporating Ga atoms into the AlAsSb multiplication layer serves to mitigate the degree of oxidation on the AlAsSb surface. This can prove beneficial during the manufacture of devices for mesa structures, particularly during the etching process.

On the other hand, such stoichiometry can affect the DC performance of devices. By increasing the Ga atom percentage in AlAsSb stoichiometry, quaternary alloys with the formula $Al_{1-x}Ga_xAs_{0.56}Sb_{0.44}$ (x=0, 0.05, 0.1, 0.15) are synthesised. They must meet the requirement of being lattice-matched with both the InP and InGaAs layers. In this case, the alloy band-gap is reduced, as shown in Figure 27 (the red arrow from AlAsSb pointing towards $Al_{1-x}Ga_xAsSb$).

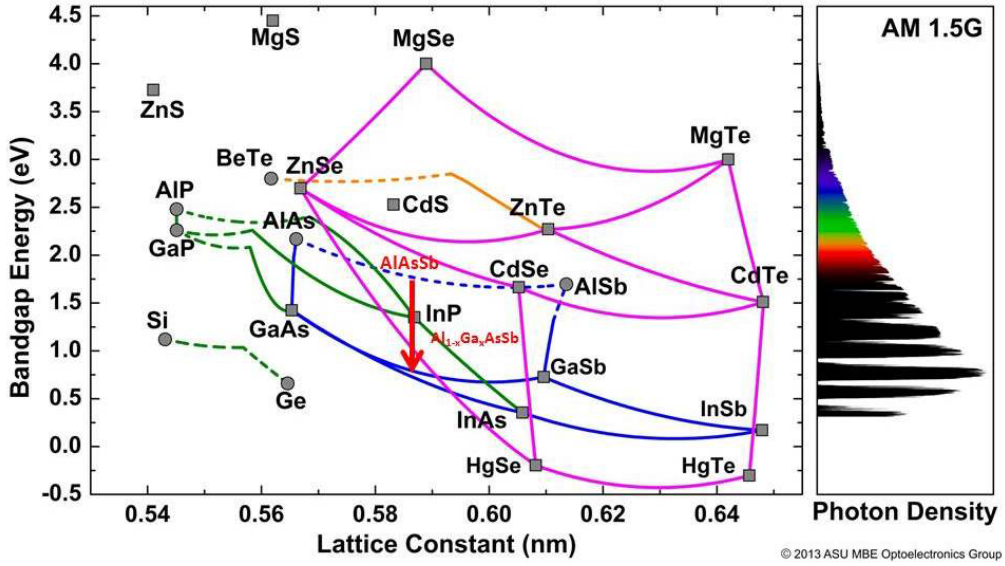

Figure 27 Band-gap energies on the basis of the lattice constant for different III-V materials

Therefore, this scenario produces the following results:

a) Mitigation of oxidation during the mesa-step process, thereby decreasing surface leakage current.

b) An increase in the probability of tunnelling via the multiplication layer, which is undesirable.

c) A decrease in the threshold voltage of the devices, as impact ionisation can be triggered under lower electric fields. This can be assessed by calculating the corresponding impact ionisation factors, alpha and beta, for each individual layer.

5.2 Device manufacture

Four different wafers were studied. The stoichiometry of each individual wafer is provided below, and, for the sake of convenience, M433x labels will be used for descriptive purposes.

- M4333 (Ga 0%, Al 100%), M4335 (Ga 5%, Al 95%), M4338 (Ga 10%, Al 90%), M4339 (Ga 15%, 85%)

The structure of each wafer is outlined below, in Table 2.

Doping type	M4333	M4335	M4338	M4339	Thickness
	Material	Material	Material	Material	Nominal (nm)
p^+ contact	InGaAs	InGaAs	InGaAs	InGaAs	100
p^+ cladding	AlAsSb	Ga(0.05)Al(0.95)AsSb	Ga(0.1)Al(0.9)AsSb	Ga(0.15)Al(0.9)AsSb	300
i grading	AlAsSb	Ga(0.05)Al(0.95)AsSb	Ga(0.1)Al(0.9)AsSb	Ga(0.15)Al(0.9)AsSb	100
n+ cladding	AlAsSb	Ga(0.05)Al(0.95)AsSb	Ga(0.1)Al(0.9)AsSb	Ga(0.15)Al(0.9)AsSb	100
n+ contact	InGaAs	InGaAs	InGaAs	InGaAs	1000
SI Sustrate	InP	InP	InP	InP	

Table 2 Schematic summary of the epitaxial structure of the M4333, M4335, M4338 and M4339 samples

The InGaAs/AlAsSb PIN diodes were manufactured according to the standard recipe, except in the case of the chemical etching step. The etching recipe was as follows:

1) H_2SO_4:H_2O_2:H_2O (1:8:80) was employed to etch the 100nm InGaAs layer at the rate of 2.8nm/sec
2) Pure HCL was employed for 1sec to etch the $Al_{1-x}Ga_xAs_{0.56}Sb_{0.44}$ layers.

This etchant combination etched down the bottom n+ contact layer by 50-60nm. Surface oxidation proved less severe, when compared with the results outlined in

paragraph 3.3.1, but trenches did appear on the samples surfaces. This phenomenon was more pronounced on M4339 samples.

5.3 Current-voltage (IV) characteristic

IV measurements were carried out for 50um, 100um and 200um radius devices in order to determine the surface leakage or bulk current domination. IV results were scaled in area and perimeter (refer to Figure 28). Figure 29 presents the forward I-V of M433x samples for 50um, 100um and 200um radius devices. The fact that all graphs scale well along the perimeter indicates the predominant position of surface leakage current. As indicated above, this issue arises due to surface oxidation and can only be eliminated once a degree of passivation is applied to each sample. Figure 28 also allows for the extraction of an estimate of the break-down voltage. Sharp and clearly defined breakdown voltages were founded at 12.3V for M4333, 12.9V for M4335, 12.1V for M4338 and 12.5V for M4339.

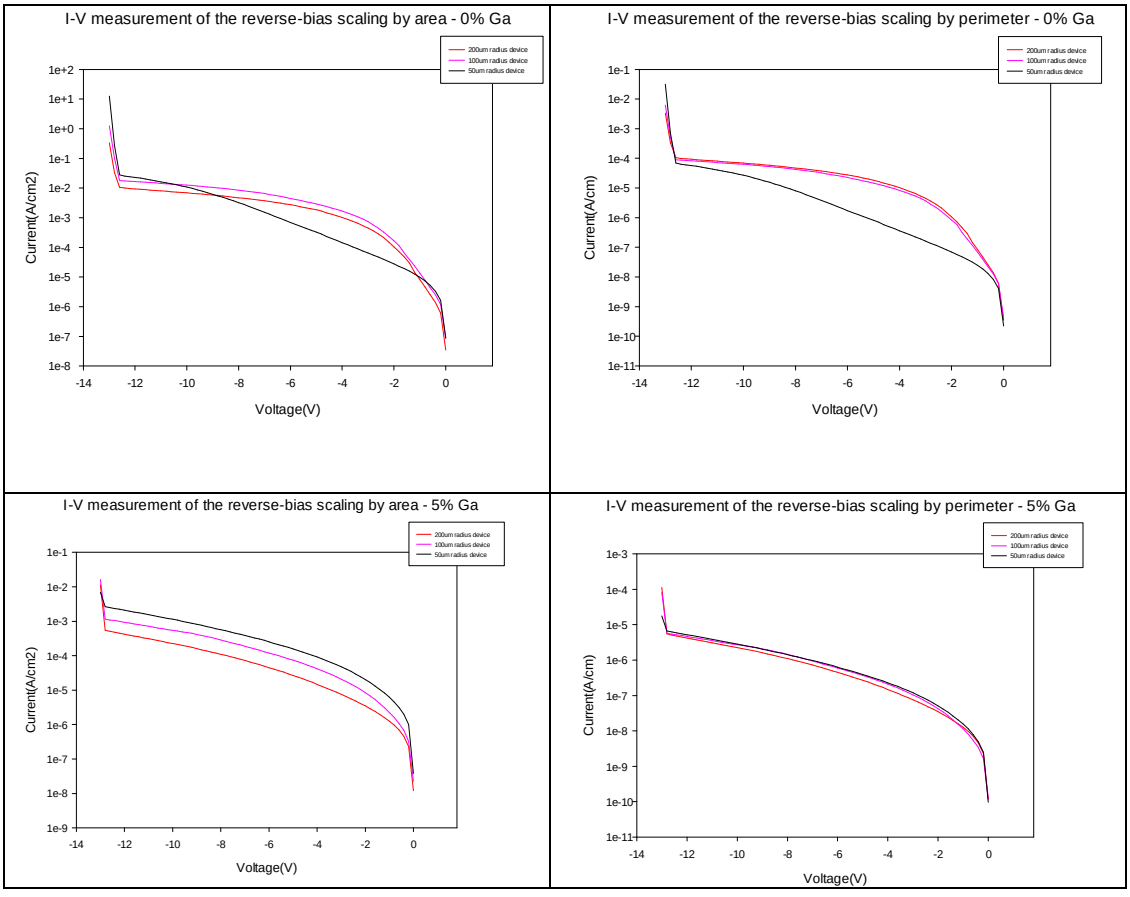

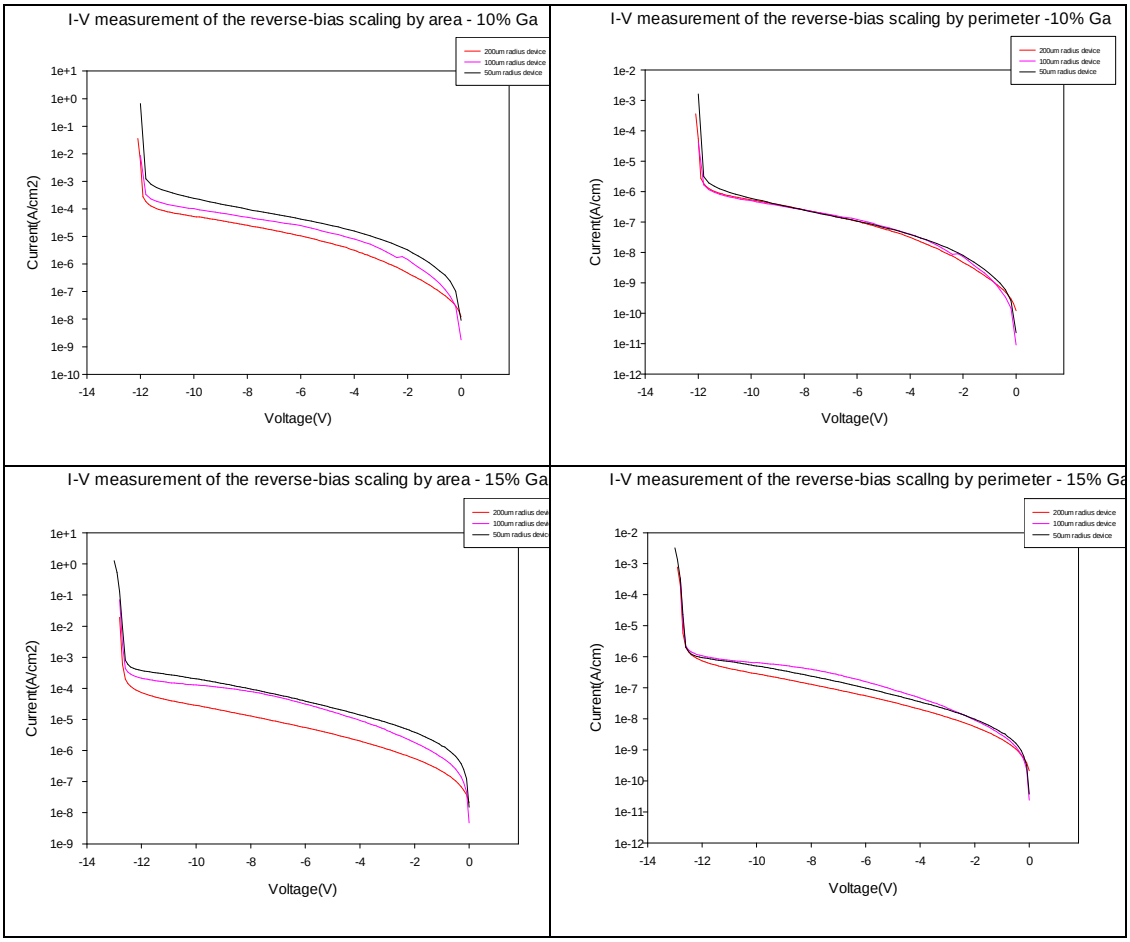

Figure 28 I-V measurement for M433x samples, scaled by area and perimeter

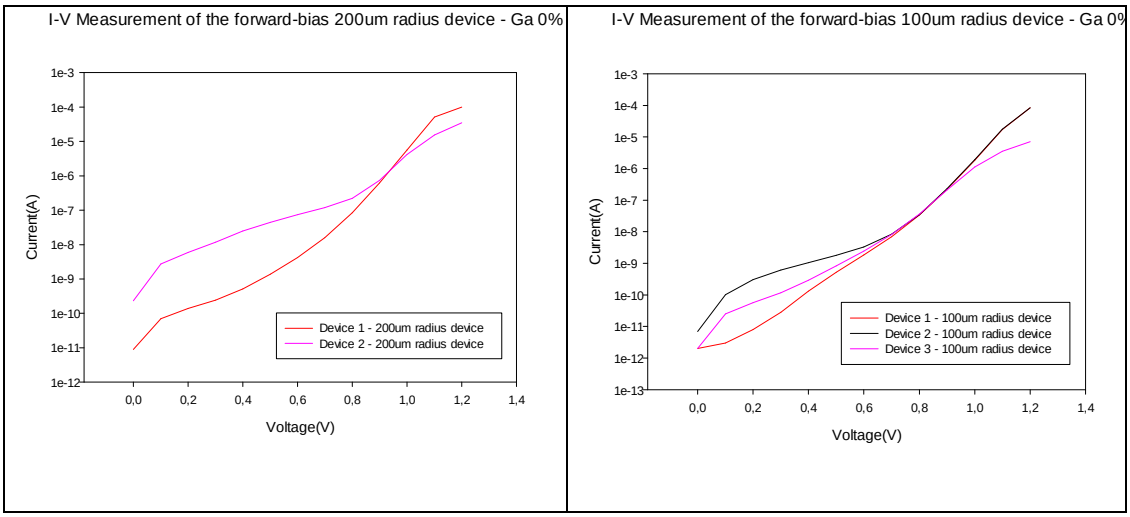

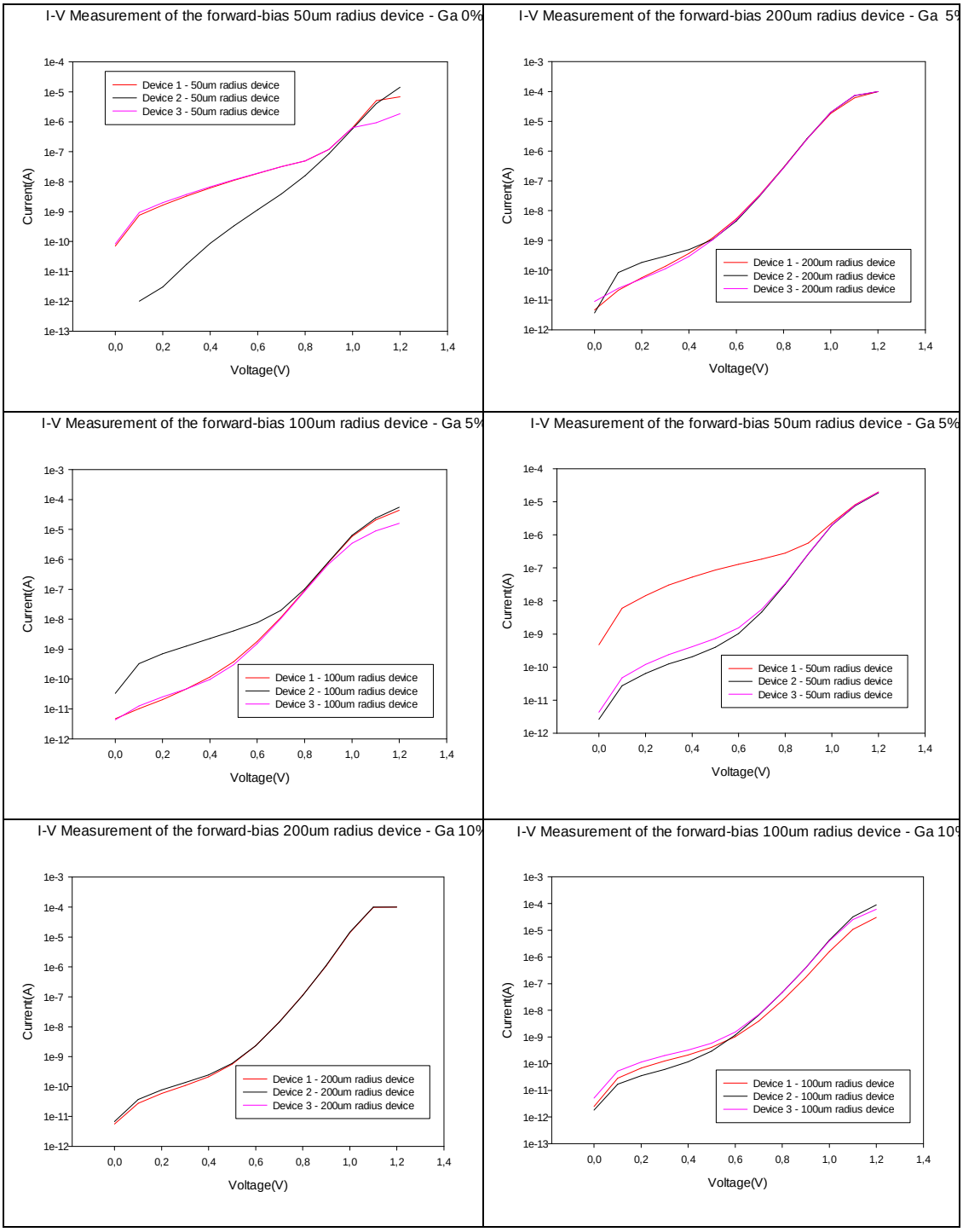
I-V Measurement of the forward-bias 50um radius device - Ga 0%
Device 1 - 50um radius device
Device 2 - 50um radius device
Device 3 - 50um radius device
Current(A)
Voltage(V)
I-V Measurement of the forward-bias 200um radius device - Ga 5%
Device 1 - 200um radius device
Device 2 - 200um radius device
Device 3 - 200um radius device
Current(A)
Voltage(V)
I-V Measurement of the forward-bias 100um radius device - Ga 5%
Device 1 - 100um radius device
Device 2 - 100um radius device
Device 3 - 100um radius device
Current(A)
Voltage(V)
I-V Measurement of the forward-bias 50um radius device - Ga 5%
Device 1 - 50um radius device
Device 2 - 50um radius device
Device 3 - 50um radius device
Current(A)
Voltage(V)
I-V Measurement of the forward-bias 200um radius device - Ga 10%
Device 1 - 200um radius device
Device 2 - 200um radius device
Device 3 - 200um radius device
Current(A)
Voltage(V)
I-V Measurement of the forward-bias 100um radius device - Ga 10%
Device 1 - 100um radius device
Device 2 - 100um radius device
Device 3 - 100um radius device
Current(A)
Voltage(V)

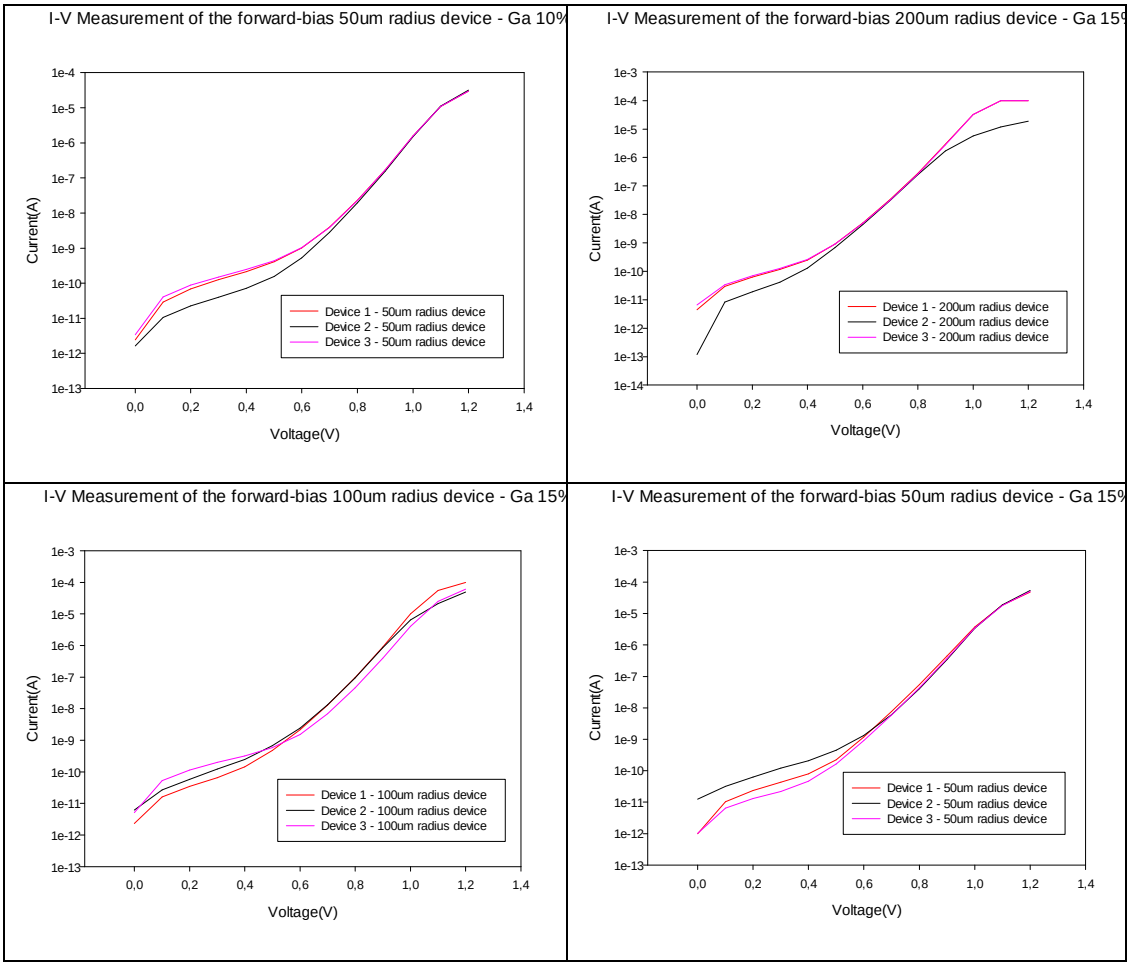

Figure 29 Forward I-V measurement for M433x samples

A dark current comparison between samples is provided in Figure 30. Three clearly distinct dark current levels are evident: the higher level (~5e-5A) corresponds to devices from the M4333 sample, the medium level (~1e-6A), to devices from the M4335 sample, and the lower level (~2.5e-7A), to devices from the M4338 and M4339 samples. This is an interesting result as it evidences a trend towards a reduction of and a saturation limit within surface-leakage current, along with increased Ga composition. That is, there is a percentage of Ga composition wherein dark-current performance does not improve.

It should be noted that all results presented in Figure 28 and Figure 30 correspond to measures carried out several months subsequent to manufacture. All measures that were carried out close to the date of manufacture did not display any evidence of the aforementioned trend. Figure 31 presents two IVs graphs. The one on the left-hand side relates to measurements taken on the date of manufacture, whilst the one on the

right-hand side involves measurements taken several months subsequent to this date. The first graph (*05-12-2013*) displays a weak difference in the dark current when the Ga composition is changed. On the other hand, in the second graph (*07-04-2014*) we can observe a strong variation of the dark current when the Ga composition is increased. Comparison of the two graphs draws to light severe degradation of the M4333 sample, non-variance in the case of the M4335 sample and a significant improvement with regards to the M4338 and M4339 samples. These results can be explained by taking into account that adding Gallium composition to AlAsSb alloys promotes reaction-limited oxidation of the device side-wall, avoiding the surface dark current degradation [28]. Therefore, the severe degradation of M4333 can be attributed to the faster oxidation rate over the same period.

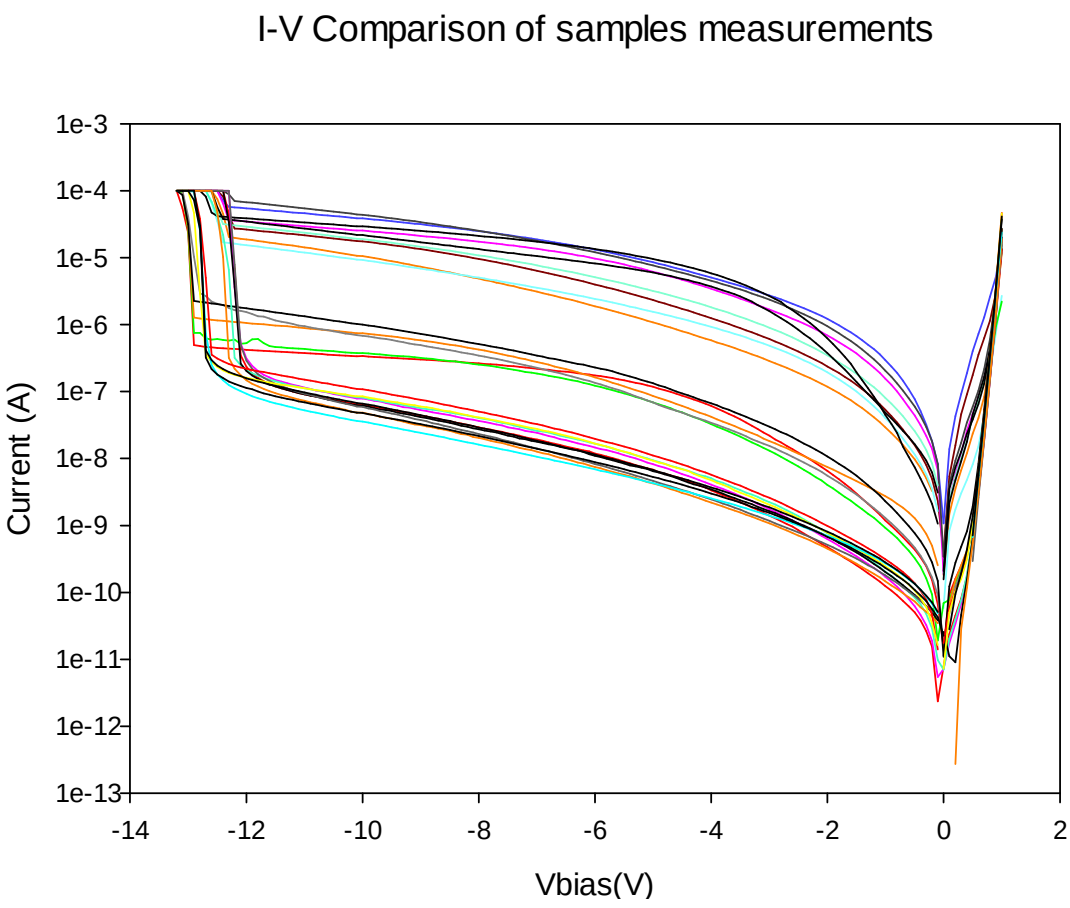

Figure 30 I-V comparison of M433x samples for 200um radius devices

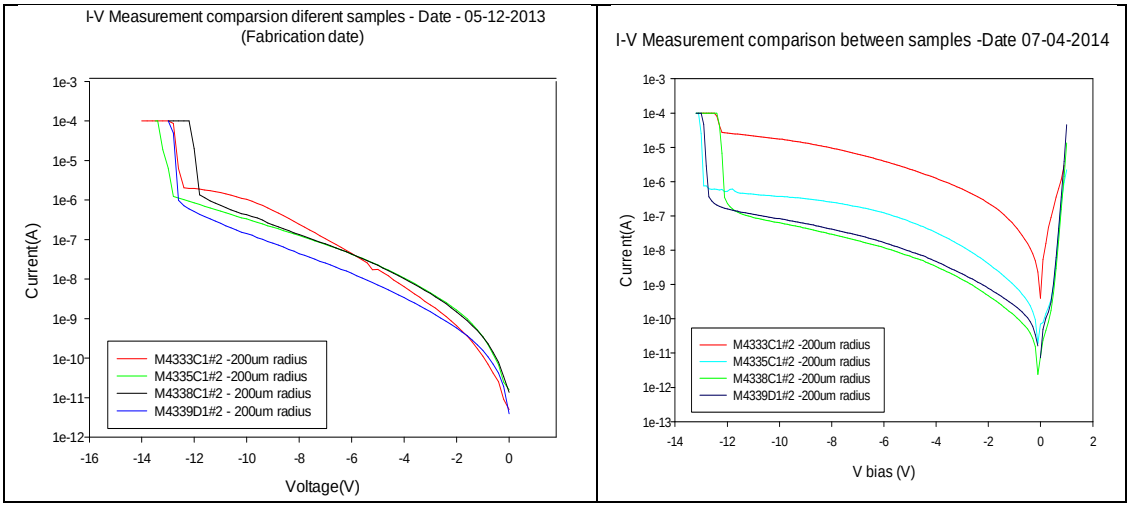

Figure 31 I-V comparison of M433x sample measurements taken on the day of the manufacture and several month later

5.4 Capacitance-voltage (CV) characteristic

CV measurements of 200um radius devices were carried out in each M433x sample. Figure 32 presents all the CV measurements, along with the fitting curves based on Poisson's equation model, cited in paragraph 3.2. Standard parameters employed for the simulation entailed a built-in potential of 1 V and a dielectric constant of 10.95. The dielectric constant is derived from linear interpolation between AlSb and AlAs [29] and it has been applied to all samples based on the assumption that Ga incorporation would not significantly alter this value. The fitted values of the M433x samples are outlined in Figure 33.

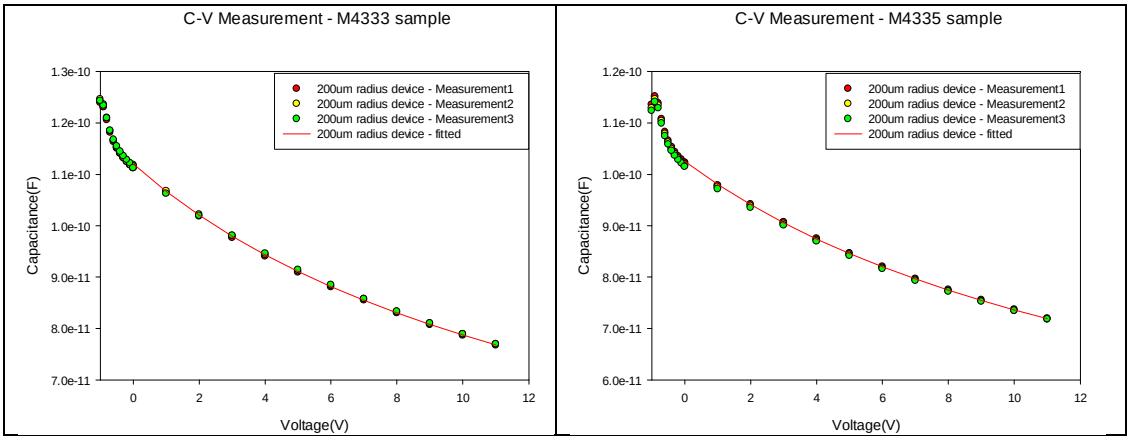

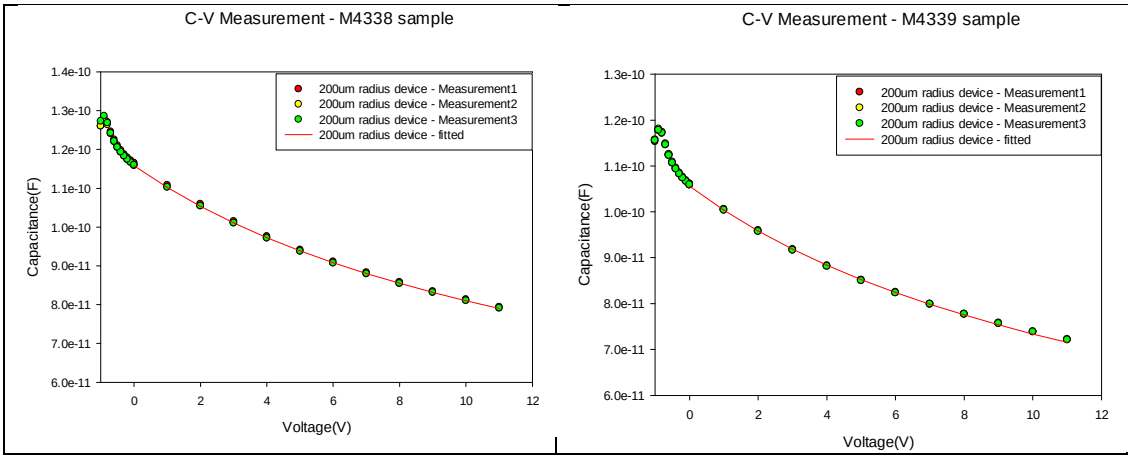

Figure 32 C-V measurements and fitted curve for M433x samples

Wafer	Thickness (nm)	Composition	Doping (cm-3)		Growth notes	Fitted Doping (cm-3)	Fitted Thickness (nm)
M4333	100	In0.53 Ga0.47 As	p	5.00E+18			
	300	Al As0.56 Sb0.44	p	2.00E+18		2E+18	
	100	Al As0.56 Sb0.44	i	1.00E+15		1E+15	103
	100	Al As0.56 Sb0.44	n	2.00E+18		2E+18	
	1000	In0.53 Ga0.47 As	n	5.00E+18			
InP n-type (2-5)E+17							
M4335	100	In0.53 Ga0.47 As	p	5.00E+18			
	300	Al0.95 Ga0.05 As0.56 Sb0.44	p	2.00E+18		2.10E+18	
	100	Al0.95 Ga0.05 As0.56 Sb0.44	i	1.00E+15	As: 61%	1E+15	102
	100	Al0.95 Ga0.05 As0.56 Sb0.44	n	2.00E+18		2.4E+18	
	1000	In0.53 Ga0.47 As	n	5.00E+18			
InP n-type (2-5)E+17							
M4338	100	In0.53 Ga0.47 As	p	5.00E+18			
	300	Al0.9 Ga0.1 As0.56 Sb0.44	p	2.00E+18		2E+18	
	100	Al0.9 Ga0.1 As0.56 Sb0.44	i	1.00E+15	As: 66%	1E+15	99.5
	100	Al0.9 Ga0.1 As0.56 Sb0.44	n	2.00E+18		2E+18	
	1000	In0.53 Ga0.47 As	n	5.00E+18			
InP n-type (2-5)E+17							
M4339	100	In0.53 Ga0.47 As	p	5.00E+18			
	300	Al0.85 Ga0.15 As0.56 Sb0.44	p	2.00E+18		1.7E+18	
	100	Al0.85 Ga0.15 As0.56 Sb0.44	i	1.00E+15	As: 66%	1E+15	109
	100	Al0.85 Ga0.15 As0.56 Sb0.44	n	2.00E+18		1.7E+18	
	1000	In0.53 Ga0.47 As	n	5.00E+18			
InP n-type (2-5)E+17							

Figure 33 Fitted values from the C-V measurement of the Al(1-x)Ga(x)AsSb PIN diodes (M433x samples)

5.5 Photo-multiplication characteristic

Avalanche gain measurements were carried out by employing a 633nm wavelength laser. A phase sensitive setup was used, with a basic structure that is detailed in paragraph 3.3. Normalisation of the avalanche gain was carried out at low bias. The gain of each sample is shown in Figure 34. Breakdown voltages were extracted from

the graphic representation of the inverted gain (*1/M*). Table 3 presents the break-down voltage (V_{bd}) obtained and the electric field modelled by Poisson's equation.

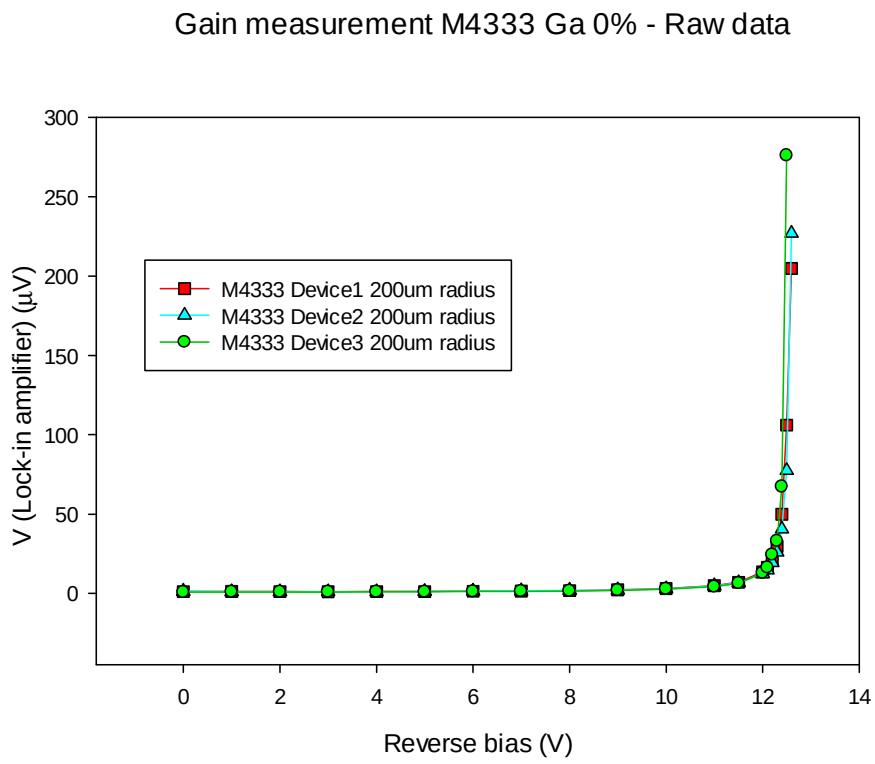

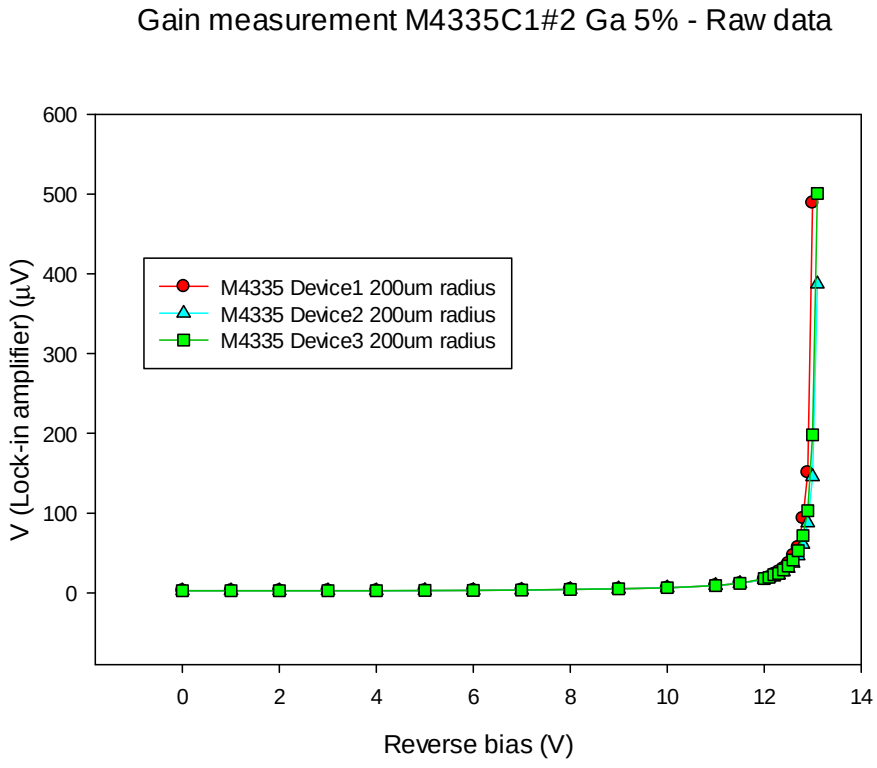

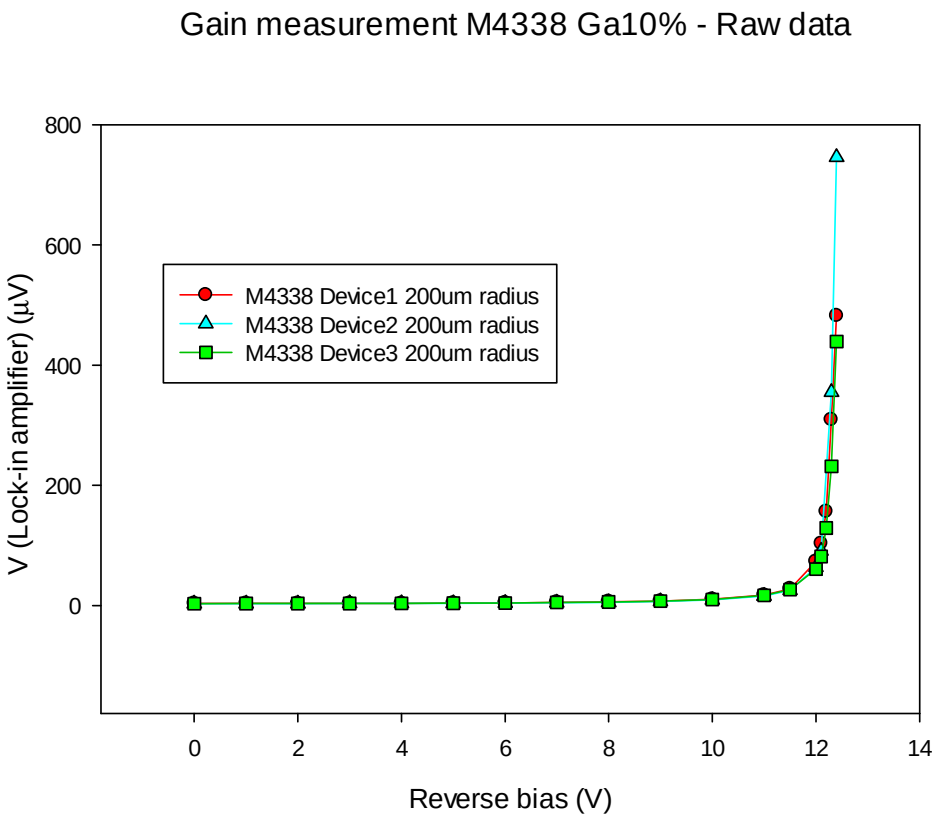

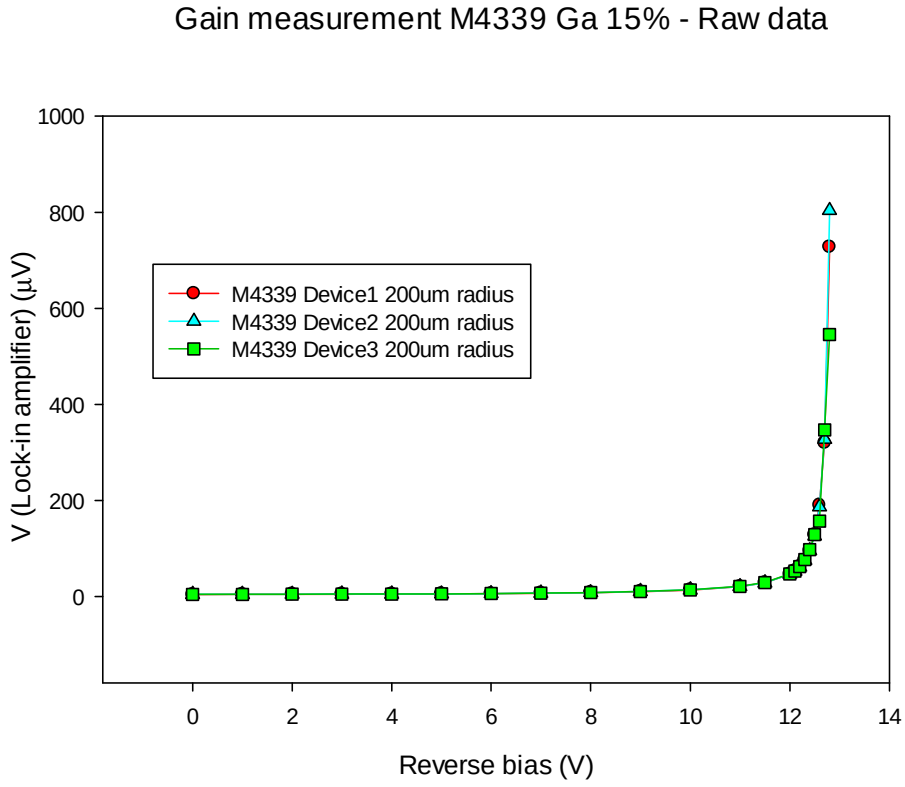

Figure 34 Gain measurement (raw data) from M433x samples that are illuminated with a 633nm wavelength laser

Gain measurement M4333 - Ga 0%

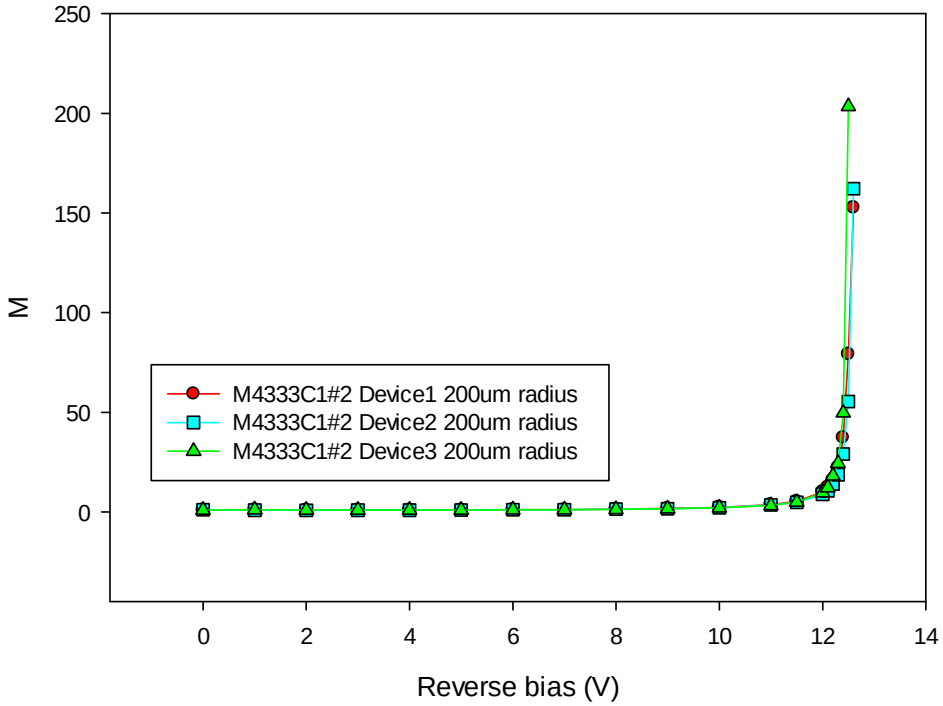

Gain measurement M4335 - Ga 5%

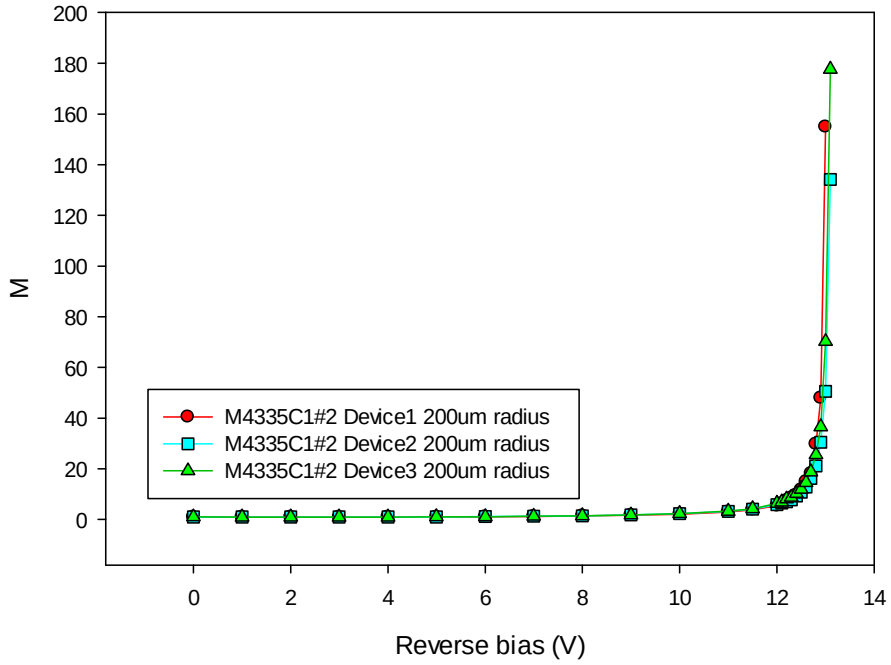

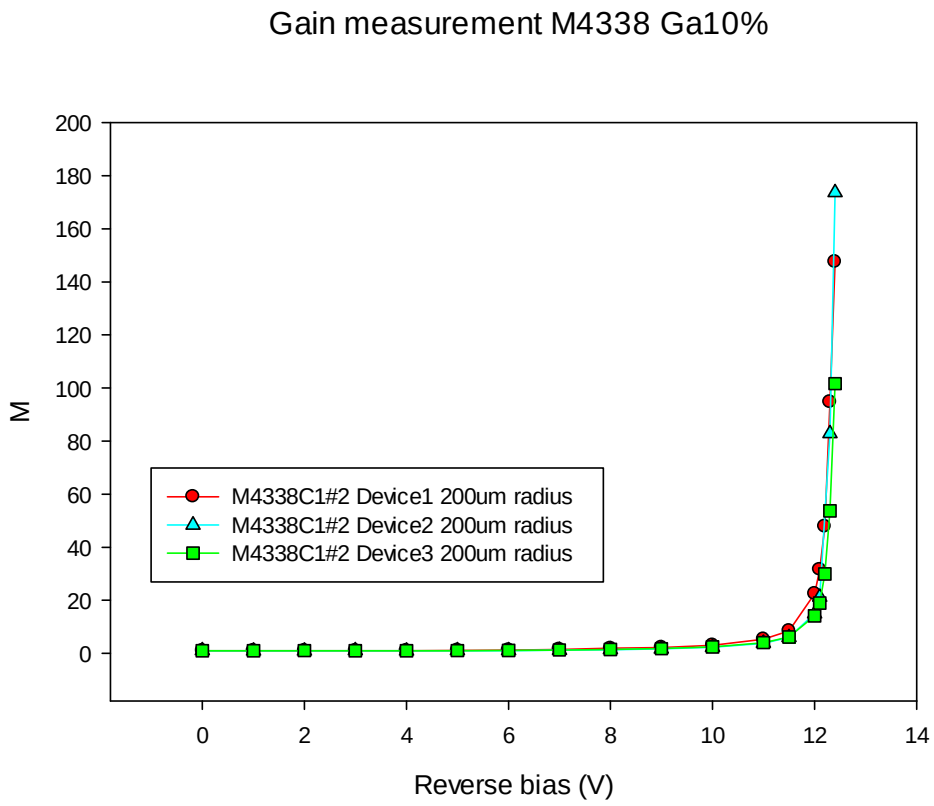

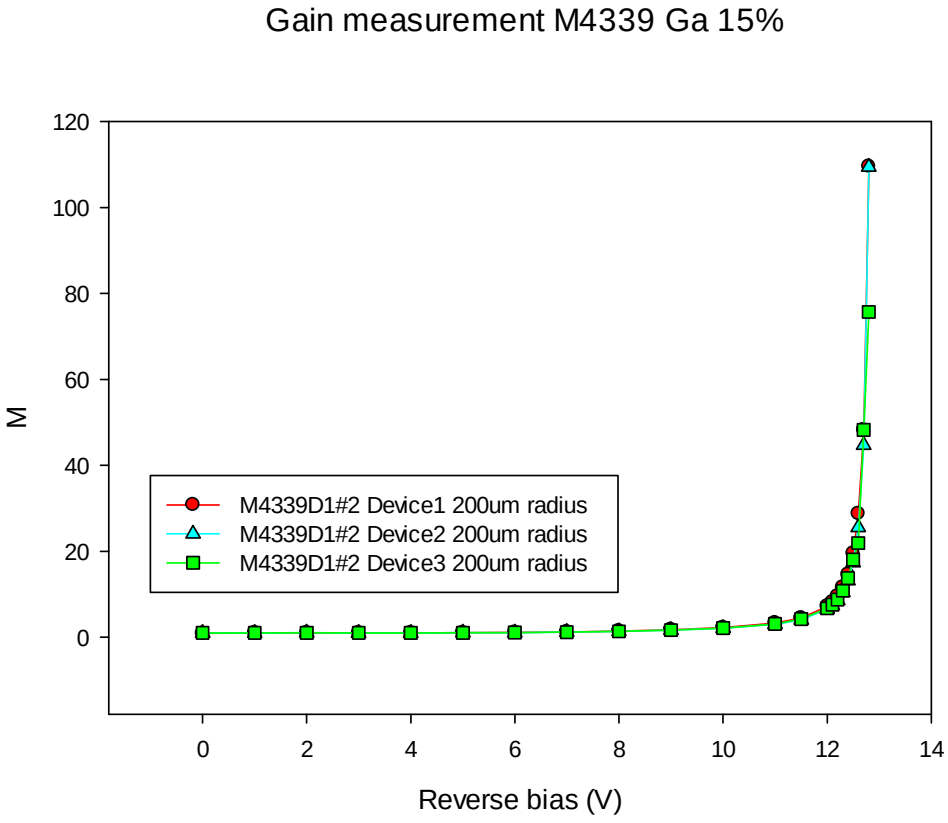

Figure 35 Gain measurement (normalised) from M433x samples that are illuminated with a 633nm wavelength laser

1/M graph M4333 - Ga 0%

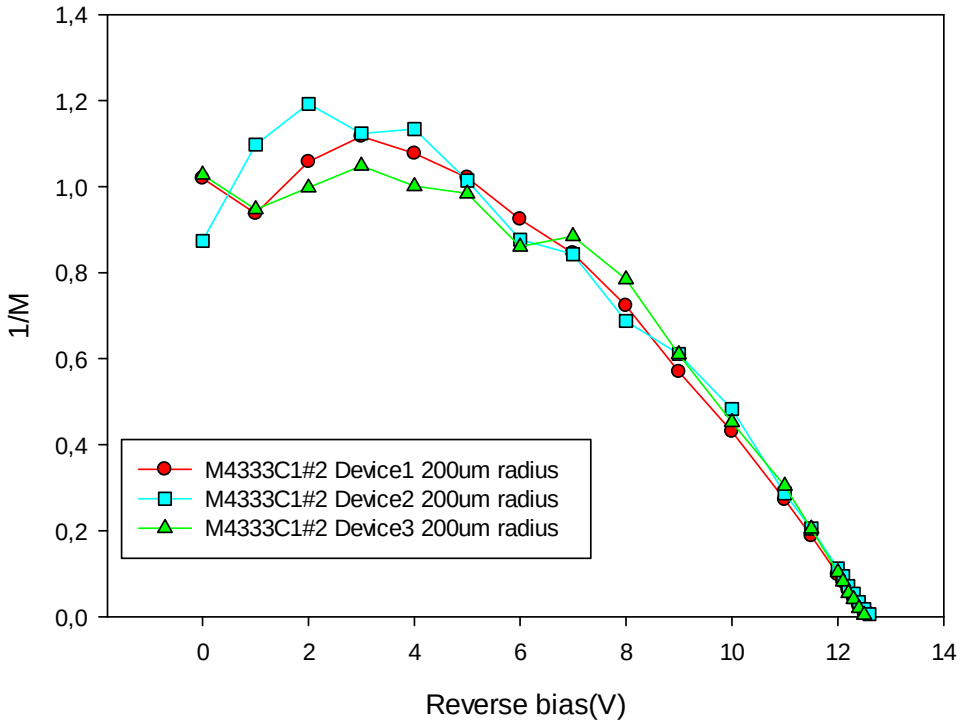

1/M graph M4335 - Ga 5%

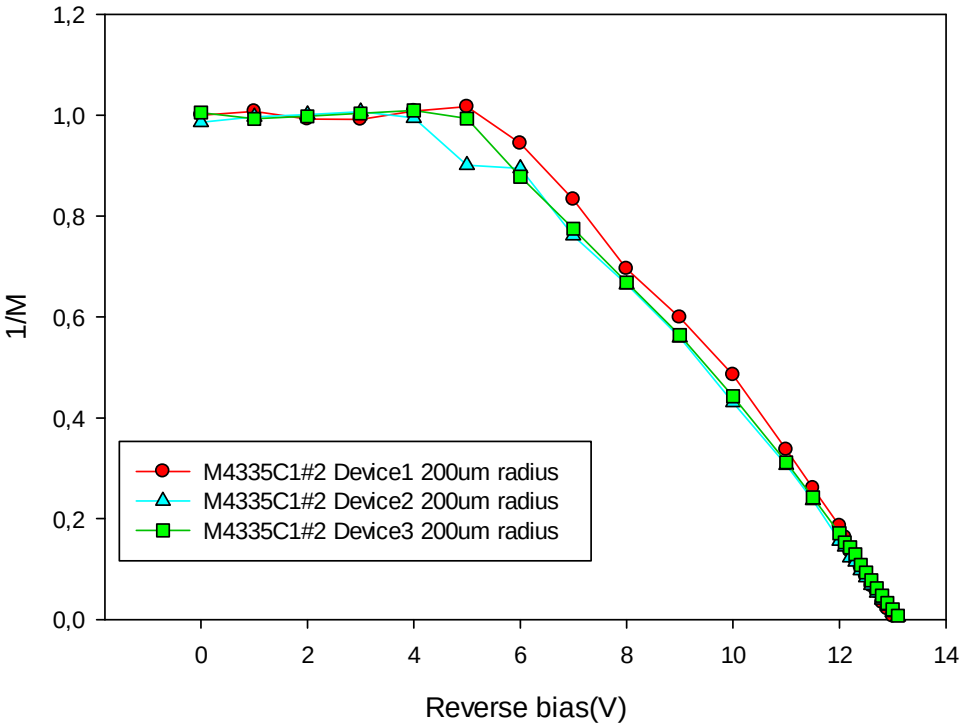

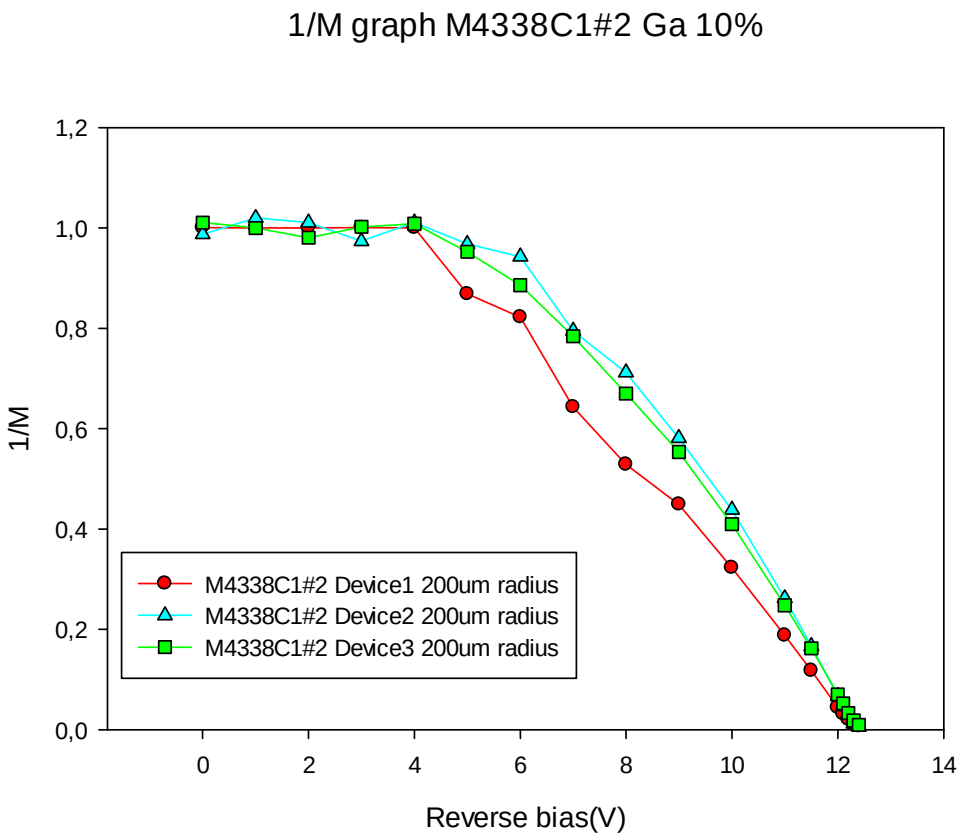

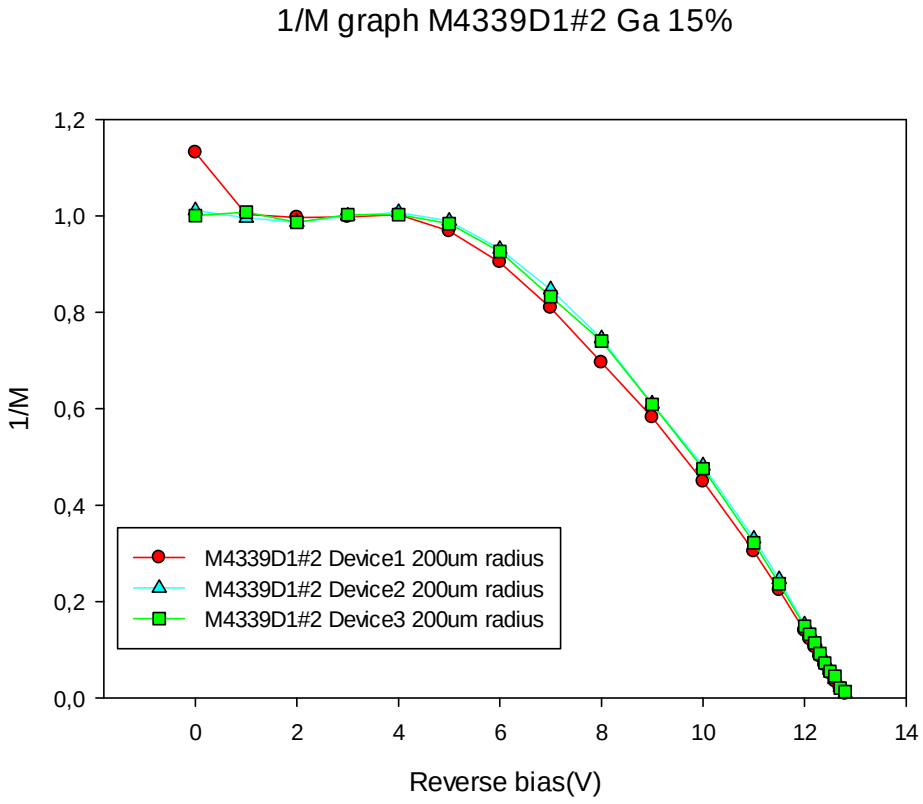

Figure 36 Inverted gain (1/M) from M433x samples that are illuminated with a 633nm wavelength laser

Ga (%)	*Sample Id*	*V_{bd} (V)*	*Electric field at V_{bd} (V/cm)*
0	M4333	12.56	1.01E+06
5	M4335	13.08	1.08E+06
10	M4338	12.42	1.03E+06
15	M4339	12.82	9.64E+05

Table 3 Breakdown voltage obtained from 1/M extrapolation and the electric field (at V_{bd})

In order to clarify the results outlined in Table 3, Figure 37 presents a bar diagram wherein the electric field is contrasted with Gallium composition. As expected, the electric field drops as Gallium composition increases. The decrement of threshold energies has bearing on this situation. Where Ga composition is increased, the band-gap also increases, whereby less electric field is required to initialise an impact ionisation event. However, where Ga composition reaches 0%, the electric field does not display a coherent trend: its value (1.01E+06 V/cm) is lower than fields entailing 5% (1.08E+06 V/cm) and 10% (1.03E+06 V/cm) Ga compositions. At present, a satisfactory explanation of this behaviour has not been forthcoming.

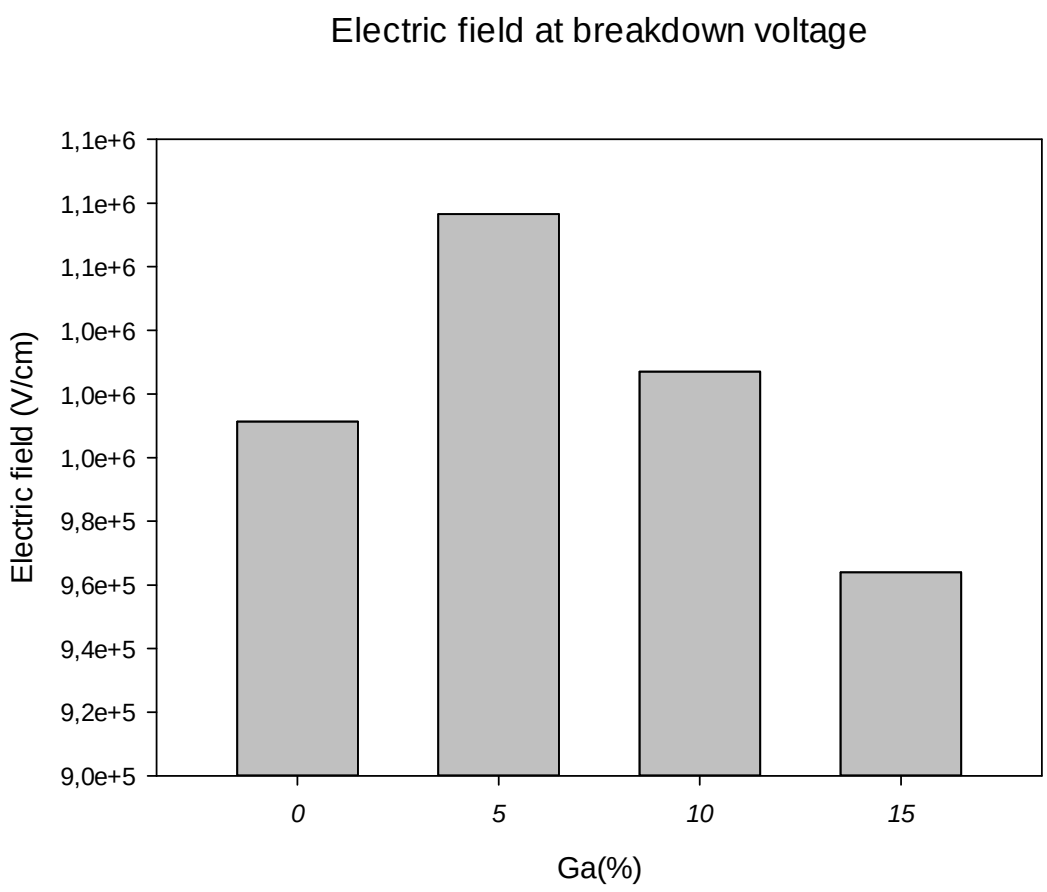

Figure 37 Bar diagram for the electric field in accordance with Gallium composition

5.6 Estimation of ionisation coefficients

The impact ionisation coefficient was extracted from each M433x sample via the local model expression. Assuming that the approximation $\alpha=\beta$ is valid, the equation (2.7b) can be expressed in the following manner:

$$\alpha = \frac{M(V)-1}{M(V)w} \tag{4.1}$$

where M(V) is the avalanche gain and w is the thickness of the i-region.

The assumption that $\alpha=\beta$ for AlAsSb alloy has been widely reported in literature [14]. For $Al_{1-x}Ga_xAs_{0.56}Sb_{0.44}$ alloys the same equivalency was adopted. To enable direct conversion between bias voltage and the electric field, it was assumed that the electrical field is constant over the entire i-region and null in the $p+$ and $n+$ cladding layers.

Taking these assumptions into consideration, Figure 38 provides an estimate of the α coefficient in accordance with the inverted electric field. To draw up this graph, the gain measurements presented in section 5.5 and the thickness values obtained in section 5.4 were employed. Furthermore, the results reported for the α coefficient of AlAsSb [16] have been plotted (straight line in the graph).

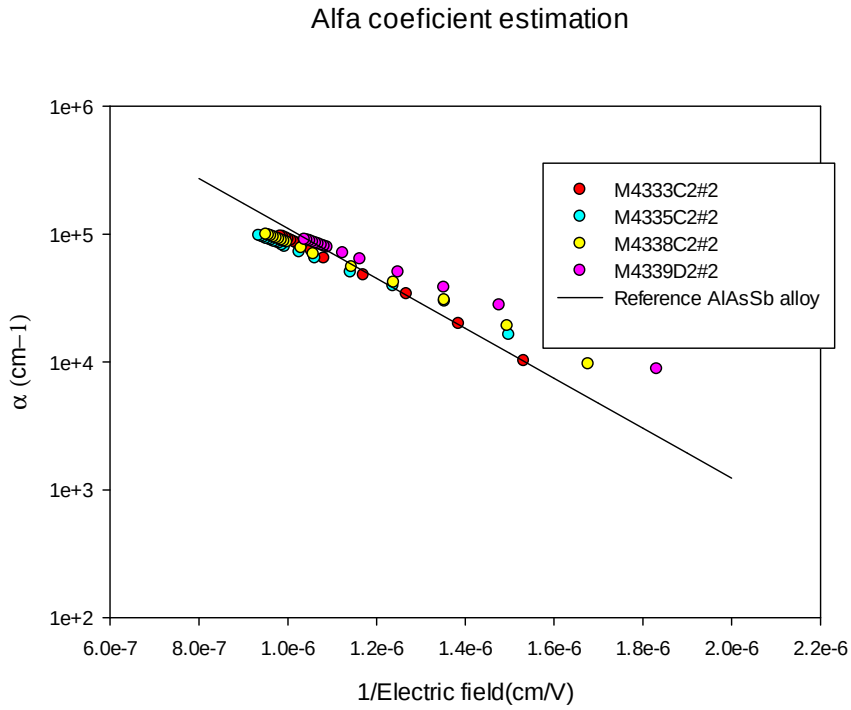

Figure 38 Alfa coefficient estimation in accordance with the inverted electric field for M433x samples

As Figure 38 indicates, the impact ionisation coefficient increases once Ga is incorporated to the alloy. As outlined above, this trend stems from the fact that the threshold energies decrease in parallel with an increment in band gap. It should be pointed out that the α coefficient obtained from the references fits well with the estimate employed in this thesis.

5.7 Spectral photo-response

Spectral photo-response was measured for all M433x samples in order to determine the band-gap of each quaternary alloy. In Figure 39 is shown the measured spectral photo-response of M433x samples. Figure 40 presents their normalised spectral response. Normalisation was carried out on the basis of the maximum absolute value of each curve. Therefore, the results are independent to the intensity of the lamp. Photo-response measurements show a clear trend towards the decrease of band-gap energy as Ga composition is increased.

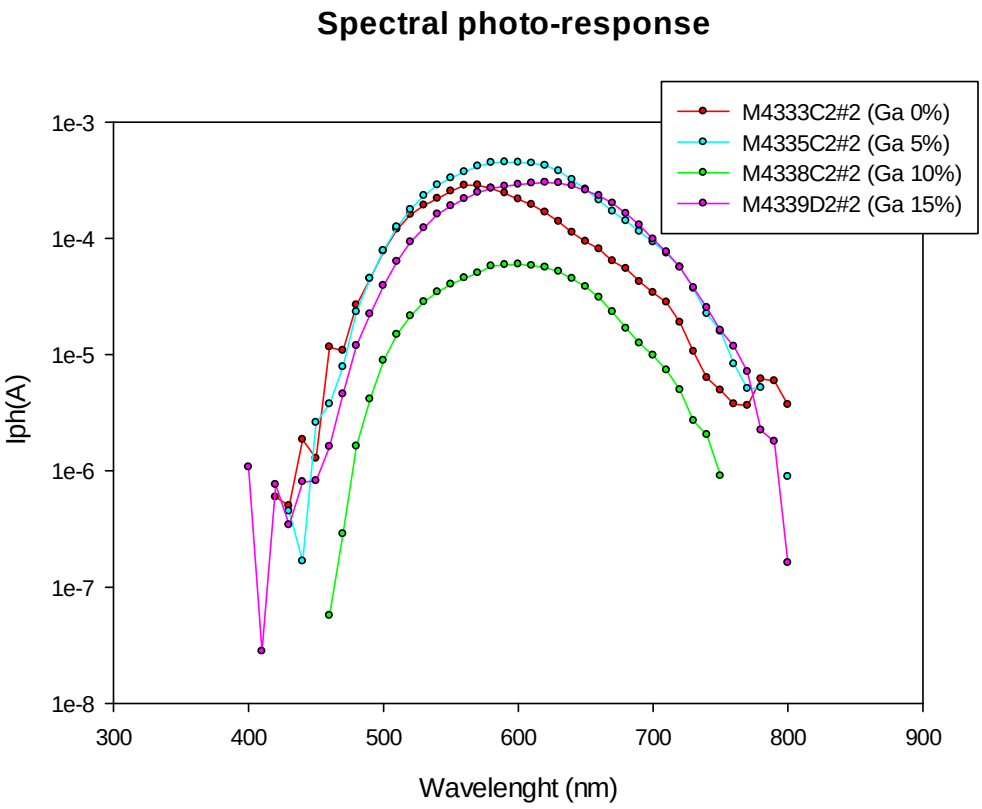

Figure 39 Measured spectral photo-response of M433x samples

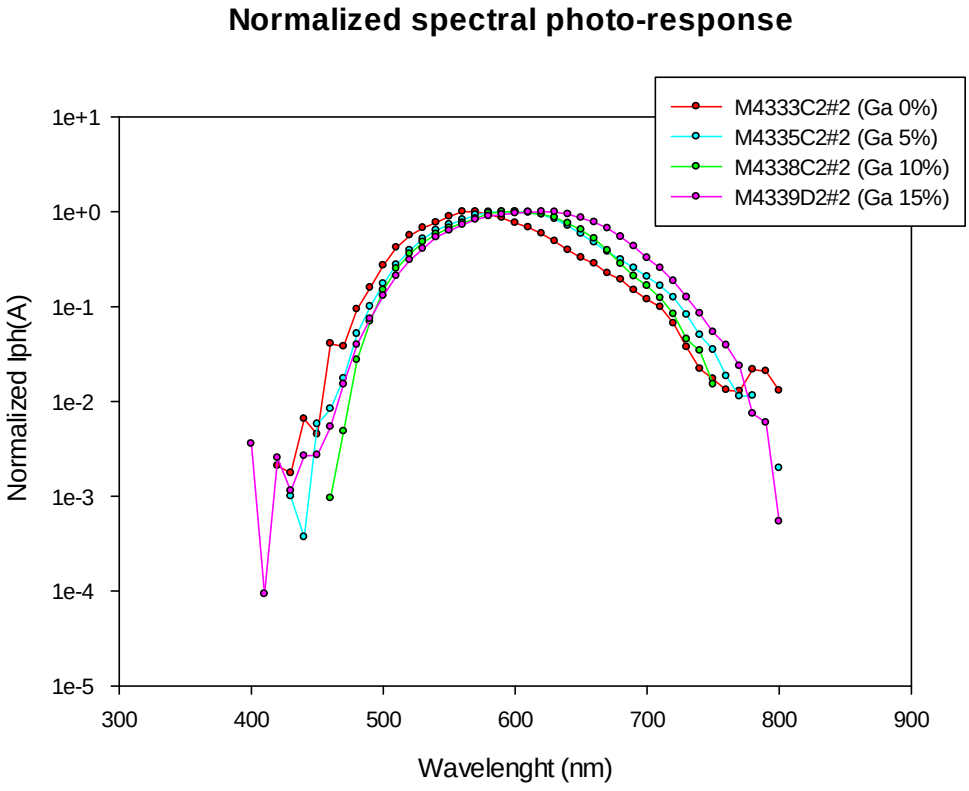

Figure 40 Normalised spectral photo-response of M433x samples

In order to extract the band-gap of each sample, equation (2.22a) can be transformed as follows:

$$E_g = \frac{hc}{\lambda_{cuttoff}} = \frac{1.24eV*um}{\lambda_{cuttoff}(um)} \quad (4.2)$$

Thus, by extracting the cut-off frequency from the graph and employing equation (4.2), the band-gap was estimated. These values are presented in Table 4.

Id sample	Ga composition (%)	$\lambda_{cut\text{-}off}$(nm)	Band-gap(eV)
M4333	0	730	1.671
M4335	5	750	1.627
M4338	10	740	1.649
M4339	15	760	1.605

Table 4 Band-gap energies for each M433x sample obtained via the spectral response

The results show a band-gap difference of 0.066 eV between 0% and 15% Ga composition. However, the trend between band-gaps obtained from M4335 and M4338 is not as we would have expected, and there is no consistent explanation from this behaviour.

5.8 Temperature dependence of the $Al_{0.85}Ga_{0.15}As_{0.56}Sb_{0.44}$ PIN diode

Section 2.3 outlines that the temperature dependence of avalanche gain can be quantified via the temperature coefficient of break-down voltage, C_{bd}. In this section, a temperature dependence study from M4339 (15% Ga) sample is presented.

I-V measurements from 200um radius devices were measured at 290K, 250K, 200K, 150K and 77K using the Janis ST-500 probe station detailed in section 3.4. Figure 41 and Figure 42 illustrates the most representative temperature dependence measurement from the M4339 (15% Ga) sample. The dark current difference between 290K and 77K in the voltage range comprising 0-12V is approximately 3-4 orders of magnitude lower. Break-down voltage is established as 12V and no tunnelling current is observed.

Forward I-V curve for the M4339 sample at different temperatures - Device (2,4,2) - 200um radius

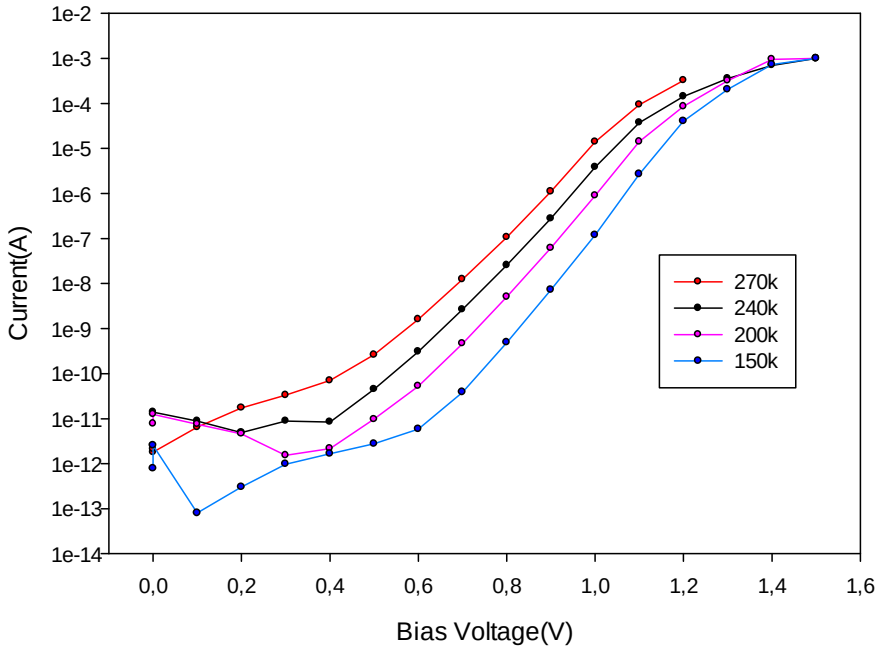

Figure 41 Temperature dependence of forward bias I-V measurement from the M4339 (15%Ga) sample

Reverse I-V curve of the M4339 sample for different temperatures - Device (2,4,2) - 200um radius

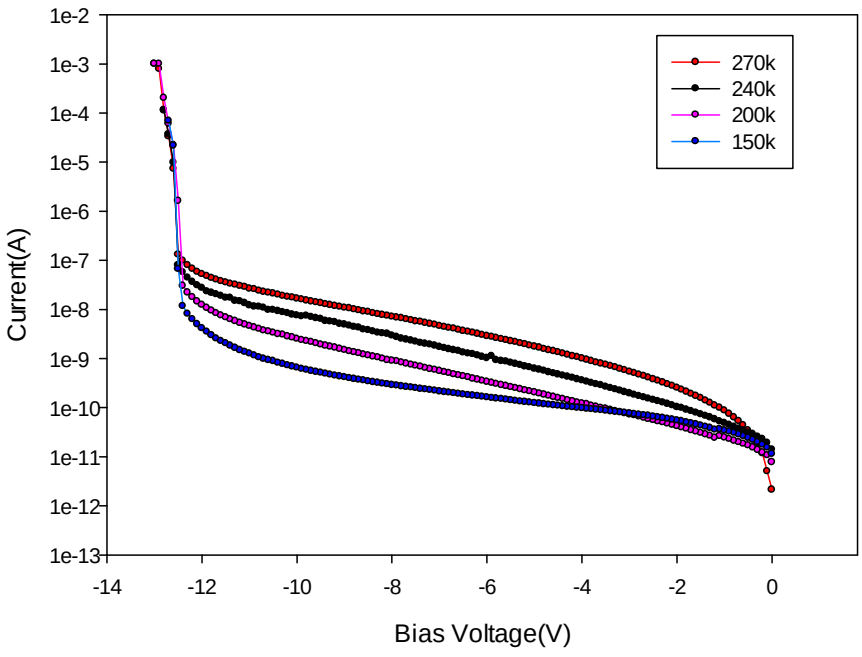

Figure 42 Temperature dependence of reverse bias I-V measurement from the M4339 (15%Ga) sample

Avalanche gain measurements were carried out on several 200um radius devices within the $Al_{0.85}Ga_{0.15}As_{0.56}Sb_{0.44}$ PIN diode at temperatures of 77, 150, 200, 240 and 270K. The set-up that was used to perform the measurements was the Janis ST-500 probe station. A 533nm green laser was included for the illumination of the devices and a phase sensitive set-up was employed to reduce noise. It should be borne in mind that care was taken to illuminate all devices in the centre, to avoid lateral light injection.

Figure 43 presents the representative results indicating the temperature dependence of avalanche gain. A more detailed graph from Figure 43 at breakdown voltage is shown in Figure 44. As expected, avalanche gain decreases in parallel with temperature reduction. Figure 45 outlines the inverted gain contrasted with reverse bias at voltages close to the avalanche breakdown. The linear regressions of each temperature were also added to the graph for extrapolation. The values extrapolated from *1/M* graph versus the temperature are presented in Figure 46. In accordance with equation (2.8), the slope of each regression line in Figure 46 corresponds to the temperature coefficient of the break down voltage, C_{bd}. The values obtained from Figure 46 are presented in Table 5.

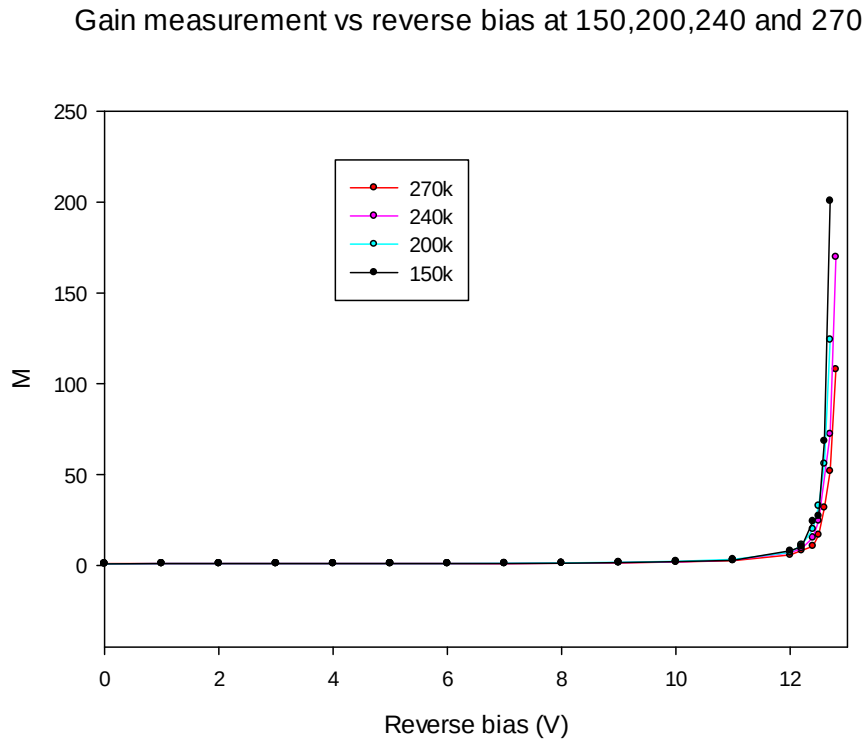

Figure 43 Temperature dependence avalanche gain from a 200um radius device within a $Al_{0.85}Ga_{0.15}As_{0.56}Sb_{0.44}$ PIN diode at 77, 150, 200, 240 and 270K

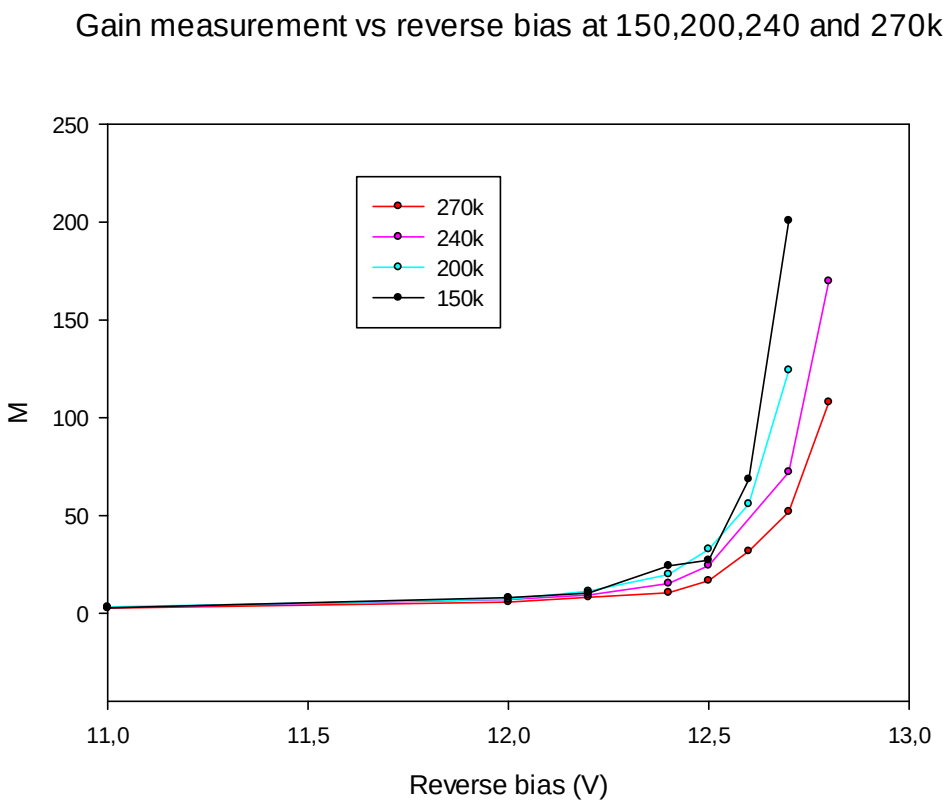

Figure 44 Detailed temperature dependence avalanche gain from a 200um radius device within a $Al_{0.85}Ga_{0.15}As_{0.56}Sb_{0.44}$ PIN diode at 77, 150, 200, 240 and 270K

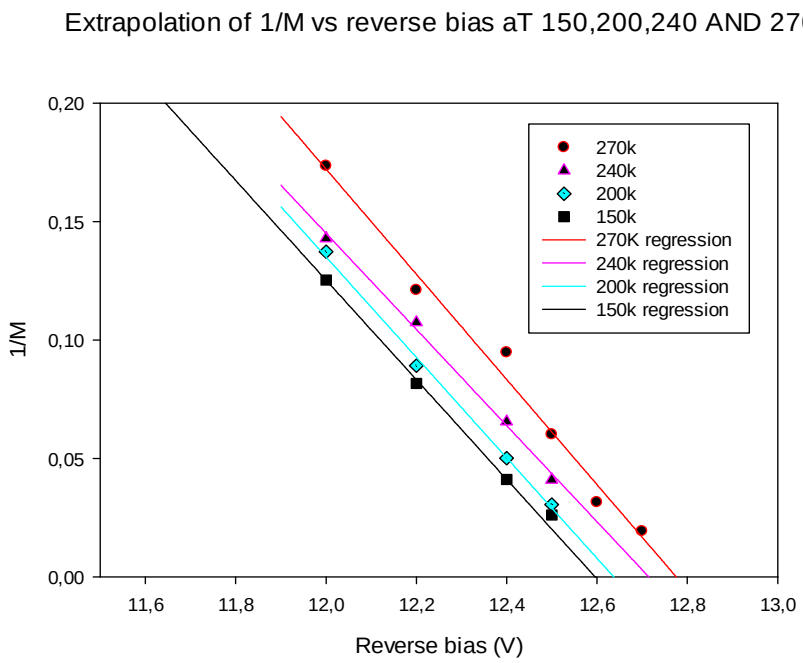

Figure 45 1/M representation at high voltage versus reverse bias from an $Al_{0.85}Ga_{0.15}As_{0.56}Sb_{0.44}$ PIN diode at 77, 150, 200, 240 and 270K. Fitted linear regression of each temperature is also shown.

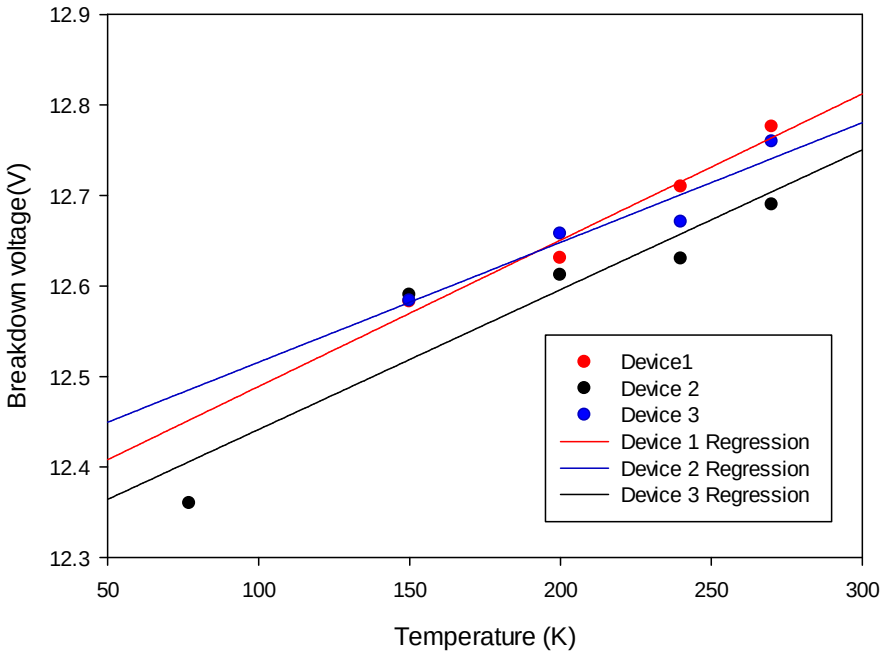

Figure 46 Breakdown voltages versus temperature for different 200um radius devices from an $Al_{0.85}Ga_{0.15}As_{0.56}Sb_{0.44}$ PIN diode

	C_{bd} (mV/K)
Device 1	1.6

Device 2	1.3
Device 3	1.5

Table 5 Temperature coefficients of break-down voltage, C_{bd}, obtained from several 200um radius devices within an $Al_{0.85}Ga_{0.15}As_{0.56}Sb_{0.44}$ PIN diode

At the time that this research was carried out, no reported results of C_{bd} from an AlAsSb PIN diode with a 100nm thick multiplication region had been reported (as was the case with the M4339 sample). Therefore, it proved impossible to establish a straightforward comparison of C_{bd} values for AlAsSb and $Al_{0.85}Ga_{0.15}As_{0.56}Sb_{0.44}$ alloys. However, there are some reported results for AlAsSb PIN diodes with 80nm thick multiplication regions [30]. These results assume that C_{bd} exhibits linear behaviour in relation to the thickness of the multiplication region thickness. An extrapolation taken from [30] provides the following equation:

$$C_{bd}\left(\frac{mV}{K}, AlAsSb\ pin\right) = 3.467x10^{-3}w(nm) + 0.6727 \qquad (4.3)$$

where w is the thickness of the multiplication layer. Via equation (4.3), where w=100nm, a value of C_{bd}= 1.02 mV/K was obtained. When comparing the C_{bd} of AlAsSb PIN diode and of the M4339 sample (15% Ga), it can be seen that the latter has a higher value (1.47 mV/K). This is consistent with what was expected, given that M4339 has a lower band-gap, and is therefore more severely affected by the phonon scattering rate.

5.9 Conclusions

This chapter presents an electrical and optical characterisation of $Al_{1-x}Ga_xAs_{0.56}Sb_{0.44}$ PIN diodes for Gallium compositions of 0%, 5%, 10% and 15%.

IV measurements at room temperature indicate that all samples evidence surface leakage current domination. This issue is explained on the basis of mesa sidewall oxidation derived from the high level of Al- compound in the alloy. Comparison between samples shows that there is a significant decrease in dark current level (~2.5 magnitude order lower) as the percentage of Gallium is increased. Indeed, it has been

found that a maximum percentage of 10% of Gallium composition saturates the minimum achievable dark current (~2.5e-7A).

CV and avalanche gain measurements were carried out in order to determine the relationship between the electric field and the percentage of Gallium composition. At first approximation, the electric field decreases in parallel with the Ga percentage. However, it should be noted that the M4333 sample (0% Ga) was contradicted initial assumptions. The reason for this inconsistency has not yet been ascertained.

Furthermore, the ionisation coefficient for each sample was estimated. Assumptions such as $\alpha=\beta$ and the confinement of the electric field only in the multiplication layer were adopted in order to simplify calculations. The results indicate that the ionisation coefficient increases in parallel with the Ga composition percentage.

Spectral photo-response was carried out to obtain an approximation of the band-gap. The following results were obtained: Eg= 1.671, 1,627, 1,649 and 1.605 eV from M4333 (0% Ga), M4335 (5% Ga), M4333 (10% Ga) and M4333 (15% Ga), respectively.

Finally, a detailed temperature dependence study of the $Al_{0.85}Ga_{0.15}As_{0.56}Sb_{0.44}$ PIN diode (M4339) was carried out. No tunnelling current was detected via the I-V measurement at low temperatures. Gain measurements were carried out to extract an estimate of the temperature coefficient of the break-down voltage, C_{bd}. The mean value obtained was C_{bd}=1,47 mV/K. This value is higher in comparison with the estimate for the AlAsSb PIN diode. Effectively, this result is consistent given that the reduction of the band-gap entails a decrease of the hot carrier population.

6. Future work and final conclusion

6.1 High speed devices

Section 1.3 indicates that is necessary to reduce the thickness of the multiplication layer as much as possible in order to increase GPB. To date, the best reported GPB for a SAM ADP pertains to an InGaAs/InAlAs structure. However, in this case GPB is still limited to 140-220 GHz [31,32,33] and the excess noise obtained was probed to improve only slightly in comparison with InGaAs/InP SAM APDs. The minimum multiplication layer thickness found in InGaAs/InAlAs SAM APDs that achieves the lowest excess noise without significant tunnelling of current is presumed to be 150nm [2]. This last design yields operation of 10 Gb/s in term of the best sensitivity.

The main objective of this thesis it is to develop an innovative SAM APD photo detector that can achieve GPB far beyond 200 GHz and an operating bandwidth of over 10 GHz. This new technology, as indicated above, will be accomplished via the use of a wide band-gap material (AlAsSb) in the multiplication layer. In order to achieve prior GPB and bandwidth values, it is expected that this innovative SAM APD will require a multiplication thickness of less than 50nm.

Beyond this scenario several issues arise. From the point of view of the material properties, AlAsSb is an –Al containing alloy that oxidises very readily when exposed to air. This condition implies a very high surface leakage current that cannot easily be resolved. On the other hand, the standard wet and dry etch procedures employed during the mesa step formation has been shown to cause premature edge break down. This is due to the high and uncontrollable etching rate of AlAsSb alloy. Both issues have been addressed in this thesis.

Section 4 outlines several wet and dry etch schemes in an attempt to resolve the issue of premature edge break down. However, all trials proved unsuccessful, either because the SEM pictures evidenced serious undercut problems, or because the chemicals proved incapable of etching the structure.

A surface leakage current scheme was presented in section 5. A series of $Al_{1-x}Ga_xAs_{0.56}Sb_{0.44}$ PIN diodes with Gallium compositions of 0%, 5%, 10% and 15% were produced and characterised. The inclusion of Gallium composition within AlAsSb alloy has been shown to be promising in terms of reducing leakage current, as borne out by the dark current measurements. Another interesting result was observed on the basis of the estimation of impact ionisation coefficients, which increase in parallel with an increment of the Ga composition. Future works should focus on the inclusion of Ga composition in new SAM APDs.

Other issues relating to device manufacture must be taken into account. As indicated in section 2.6, the RC limited bandwidth is the main contributing factor to the degradation of bandwidth within a high speed device. From the point of view of manufacture, the series resistance, R, is the key feature to be minimised. It is determined mainly by the upper metallic contact of the device. Therefore, different metallic contact process schemes should be tested in order to diminish resistance as much as possible.

Finally, the innovative SAM APD structure presents a number of technological issues that must be resolved. As indicated in 2.1, in a SAM APD, the charge sheet layer is placed between the absorption layer and the multiplication layer to control their electric-field difference. To achieve a large difference within the electric fields, the doping level of the charge sheet must be sufficiently high. However, this has been shown to prove very difficult when it is grown in a MBE machine. Several new structures must be evaluated during this thesis to allow the grower to calibrate a successful doping level for the charge sheet layer.

6.2 Measurement of the excess noise of InGaAs/AlAsSb SAM APDs.

As discussed in section 1.3.1, the thickness of the multiplication layer must be reduced in order to decrease excess noise. This issue is linked to the dead-space effect cited in section 2.5. The measurement the excess noise of AlAsSb SAM APDs with a 40nm thick multiplication layer has been reported to be very low (k_{eff} ~0.1 to 0.15) [13]. Therefore, AlAsSb material becomes a viable option for low-noise APD application.

As this thesis is dealing with a new AlAsSb material for the manufacture of APD devices, it is useful to characterise excess noise in order to compare performance with reported results.

6.3 Temperature dependence of InGaAS/AlAsSb SAM APDs.

Section 2.3 has indicates the importance of temperature dependence when characterising APDs. The two key features of temperature dependence were also presented: the coefficient of the breakdown voltage, C_{bd}, and activation energy, E_a. The first parameter, C_{bd}, determines the temperature dependence of the breakdown voltage, whilst activation energies, E_a, allow for deep analysis of the components that make up dark current.

The temperature dependence results for the $Al_{0.85}Ga_{0.15}As_{0.56}Sb_{0.44}$ PIN diode sample are presented in section 5.8. However, more gain and dark current measurements should be carried out for the other Ga composition samples in order to establish any trend.

On the other hand, dark current measurement analysis must be carried out for the InGaAsSb/AlAsSb SAM APDs under review in this thesis. Activation energy extraction, E_a, will allow us to determine the domination mechanism within the bulk and surface current components as well as the existing traps in the structure.

7. References

[1] R. J. McIntyre, “Multiplication Noise in Uniform Avalanche Diodes”, IEEE Transaction on electron devices, vol. ED-13, No. 1, 1966.

[2] D. S. Ong, K. F. Li, G. J. Rees, J. P. R. David, and P. N. Robson, “A simple model to determine multiplication and noise in avalanche photodiodes,” J. Appl. Phys., 83(6), pp. 3426-3428, 1998.

[3] J. Beck et all, “The HgCdTe Electron Avalanche Photodiode”, Journal of Electronic Materials, Vol. 35, No. 6, 2006.

[4] A. R. J. Marshall, C. H. Tan, M. J. Steer and J. P. R. David, “Extremely Low Excess Noise in InAs Electron Avalanche Photodiodes”, IEEE Photonics Technology Letters, Vol. 21, No. 13, July 1, 2009.

[5] K. F. Li, D.S. Ong and J. P. R. David, “Avalanche multiplication noise characteristics in thin GaAs p+-i-n+ diodes”, IEEE Trans. Electron Dev., 45(10), p.2102, 1998.

[6] J. Xie, S. Xie, R. C. Tozer, C. H. Tan, Excess Noise Characteristics of Thin AlAsSb APDs.*IEEE Trans. Electron Devices*, vol. 59, no. 5: pp. 1475-1479,2012.

[7] C. H. Tan, S. Xie, and J. Xie, Low Noise Avalanche Photodiodes Incorporating a 40 nm AlAsSb Avalanche Region.*IEEE J. Quantum Electron*, vol. 48, no. 1: pp. 36-41,2012.14.

[8] http://www.cisco.com/en/US/netsol/ns827/networking_solutions_sub_solution.html#~forecast.

[9] H.-G. Bach, R. Kunkel, G. G. Mekonnen, R. Zhang and D. Schmidt, “100 Gb/s photoreceivers for coherent and direct detection”, OFC conference, paper OML1, 2011.

[10]T. Kagawa, H. Asai, and Y. Kawamura, “An InGaAs /InAlAs Superlattice Avalanche Photodiode with a Gain Bandwidth Product of 90 GHz”, IEEE Photonics Technology Lett., Vol. 3, No. t

[11]T. Kagawa, Y. Kawamura, and H. Iwamura, “InGaAsP-InA1As Superlattice Avalanche Photodiode”, IEEE J. Quantum Electron., Vol. 28, No. 6, 1992.

[12]D. S. G. Ong, M. M. Hayat, Senior Member, IEEE, J. P. R. David, Senior Member, IEEE, and J. S. Ng, Member, IEEE, “Sensitivity of high-speed lightwave system receivers using InAlAs avalanche photodiodes”, IEEE Photon. Tech. Lett.,23(4), p.233, 2011.

[13]C. H. Tan, S. Xie and J. Xie, “Low Noise Avalanche Photodiodes Incorporating a 40 nm AlAsSb Avalanche Region”, IEEE J. Quantum Electron, vol. 48, no. 1: pp. 36-41, 2012.

[14]M. A. Saleh, M. M. Hayat, Senior Member, IEEE, “Impact-Ionization and Noise Characteristics of Thin III–V Avalanche Photodiodes”, IEEE Transactions on Electron Devices, vol. 48, no. 12, 2001.

[15]J. L. Moll, and N. Meyer, Secondary Multiplication in Silicon. Solid State Electron, vol. 3: pp. 155-161, 1961.

[16]J. J. Xie, “Characterization of low noise InGaAs/AlAsSb Avalanche Photodiodes”, PhD thesis, University of Sheffield, 2013.

[17]R. Ghin, J. P. R. David, M. Hopkinson, M. A. Pate, G. J. Rees and P. N. Robson, "Impact ionization coefficients in GaInP p-i-n diodes", Appl. Phys. Lett., vol. 70, pp.3567 -3569, 1997.

[18]C. R. Crowell and S. M. Sze, “Temperature Dependence of Avalanche Multiplication in Semiconductors”, Appl. Phys. Lett., vol. 9, no. 6: pp. 242-244, 1966.

[19]C. Groves, C. N. Harrison, J. P. R. David and G. J. Rees, “Temperature dependence of breakdown voltage in AlxGa1-xAs”, J. Appl. Phys., vol. 96, no. 9: pp. 5017-5019, 2004.

[20]C. Groves, R. Ghin, J. P. R. David and G. J. Rees, “Temperature Dependence of Impact Ionization in GaAs”, IEEE Trans. Electron Devices, vol. 50, no. 10: pp.2027-2031, 2003.

[21]D. J. Massey, J. P. R. David and G. J. Rees, “Temperature Dependence of Impact Ionization in Submicrometer Silicon Devices”, IEEE Trans. Electron Devices, vol. 53, no. 9: pp.2328-2334, 2006.

[22]G. J. Rees and J. P. R. David, “Nonlocal impact ionization and avalanche multiplication”, J. Appl. Phys. D, vol 43, pp. 243001, 2010.

[23]J. E. Bowers and C. A. Burrus, “Ultrawide-Band Long-Wavelength p-i-n Photodetectors”, J. Lightwave Tech., vol. LT-5, no. 10: pp. 1339-1350, 1987.

[24]S. M. Sze, “Physics of semiconductor devices”, 2nd edition, John Wiley & Sons, Inc., pp. 84-94, 1981.

[25]M. M. Wood, W. C. Hojnson and M. A. Lampert, “Use of a schottky barrier to measure impact ionization coefficients in semiconductors”, Solid State Electron, vol. 16, no.3 :pp. 381-394, 1973.

[26]S. Xie, “Design and characterisation of InGaAs high speed photodiodes, InGaAs/InAlAs avalanche photodiodes and novel AlAsSb based avalanche photodiodes”, PhD thesis, University of Sheffield, 2012.

[27]R. L. Davies and F. E. Gentry, "Control of Electric Field at the Surface of P-N Junctions", IEEE Transactions on Electron Devices, vol. ED-11, pp.313 -323, 1964.

[28]S. K. Mathis, K. H. A. Lau, A. M. Andrews and E. M. Hall, “Lateral oxidation kinetics of AlAsSb and related alloys lattice matched to InP”, J. Appl. Phys. 89, 2458, 2001.

[29]D. W. Palmer, www.semiconductors.co.uk , 2006.

[30]S. Xie and C. H. Tan, “AlAsSb avalanche photodiodes with a sub-mV/K temperature coefficient of breakdown voltage”, IEEE J. Quantum Electron., vol. 47, no. 11: pp. 1391-1395, 2011.

[31]T. Nakata, T. Takeuchi, I. Watanabe, K. Makila and T. Torikai, “10Gbit/s high sensitivity, low-voltageoperation avalanche photodiodes with thin InAlAs multiplication layer and waveguide structure”, Electron. Lett., vol.36, no.24: pp. 2033-2034, 2000.

[32]T. Nakata, T. Takeuchi, K. Makita, Y. Amamiya, Y. Suzuki and T. Torikai, “An ultra high speed waveguide avalanche photodiode for 40-Gb/s optical receiver.”, Proc. 27th Eur. Conf. on Opt. Comm., 2001.

[33]M. Lahrichi, G. Glastre, E. Derouin, D. Carpentier, N. Lagay, J. Decobert and M. Achouche, “240-GHz Gain-Bandwidth Product Back-Side Illuminated AlInAs Avalanche Photodiodes.”, IEEE Photon. Tech. Lett., vol.22, no.18, Sep. 15: pp. 1373-1375, 2010.

8. Appendix 1: Devices structures

SAM APD 1 (REV 2) devices

Doping type	Material	Doping density		Thickness	
		Nominal (cm^{-3})	Fitted (cm^{-3})	Nominal (nm)	Fitted (nm)
p^+ contact	InGaAs	1×10^{19}	-	10	-
p^+ cladding	InAlAs	$>5\times10^{18}$	5×10^{18}	300	-
i grading	InAlGaAs (Eg ~ 1.1 eV)	$<2\times10^{15}$	1×10^{15}	50	50
i absorption	InGaAs	$<2\times10^{15}$	6×10^{15}	500	500
i grading	InAlGaAs (Eg ~ 1.1 eV)	$<2\times10^{15}$	2×10^{16}	50	50
p charge sheet	InAlAs	5×10^{17}	2.9×10^{17}	55	55
i intrinsic	InAlAs	$<2\times10^{15}$	1×10^{16}	50	50
p charge sheet	AlAsSb	1×10^{18}	4×10^{17}	44	44
i multiplication	AlAsSb	$<2\times10^{15}$	1×10^{16}	50	40
n^+ cladding	AlAsSb	$>5\times10^{18}$	5×10^{18}	100	-
n^+ contact	InGaAs	1×10^{19}	-	300	-
Semi-insulating InP					

PIN 3 (UCL 1) devices

Doping type	Material	Doping density		Thickness	
		Nominal (cm^{-3})	Fitted (cm^{-3})	Nominal (nm)	Fitted (nm)
p^+	InGaAs	5×10^{18}	-	100	-
p^+	AlAsSb	$>2\times10^{18}$	7×10^{17}	200	-
i	AlAsSb	Undoped	1×10^{15}	30	30
n^+	AlAsSb	$>2\times10^{18}$	7×10^{17}	50	-
n^+	InGaAs	5×10^{18}		1000	-
Semi-insulating InP					

M4333 PIN diode AlAs(0.56)Sb(0.44)

Purpose	Thickness (nm)	Material	Type	Doping (cm^{-3})
p^+ contact	100	In(0.53)Ga(0.47) As	p^+	$5x10^{18}$
p^+ cladding	300	AlAs(0.56)Sb(0.44)	p^+	2×10^{18}
i absorption	100	AlAs(0.56)Sb(0.44)	i	10^{15}

n^+ cladding	100	AlAs(0.56)Sb(0.44)	n^+	2×10^{18}
n^+ contact	1000	In (0.47) Ga As	n^+	5×10^{18}
Sustrate	---	InP	n	---

M4335 PIN diode Al0.95Ga0.05As(0.56) Sb(0.44)

Purpose	Thickness (nm)	Material	Type	Doping (cm^{-3})
p^+ contact	100	In(0.53)Ga(0.47) As	p^+	$5x10^{18}$
p^+ cladding	300	Al0.95Ga0.05As(0.56) Sb(0.44)	p^+	2×10^{18}
i absorption	100	Al0.95Ga0.05As(0.56) Sb(0.44)	i	10^{15}
n^+ cladding	100	Al0.95Ga0.05As(0.56) Sb(0.44)	n^+	2×10^{18}
n^+ contact	1000	In (0.47) Ga As	n^+	5×10^{18}
Sustrate	---	InP	n	---

M4338 PIN diode Al0.90Ga0.1As(0.56) Sb(0.44)

Purpose	Thickness (nm)	Material	Type	Doping (cm^{-3})
p^+ contact	100	In(0.53)Ga(0.47) As	p^+	$5x10^{18}$
p^+ cladding	300	Al0.90Ga0.1As(0.56) Sb(0.44)	p^+	2×10^{18}
i absorption	100	Al0.90Ga0.1As(0.56) Sb(0.44)	i	10^{15}
n^+ cladding	100	Al0.90Ga0.1As(0.56) Sb(0.44)	n^+	2×10^{18}
n^+ contact	1000	In (0.47) Ga As	n^+	5×10^{18}
Sustrate	---	InP	n	---

M4339 PIN diode Al0.85Ga0.15As(0.56)Sb(0.44)

Purpose	Thickness (nm)	Material	Type	Doping (cm^{-3})
p^+ contact	100	In(0.53)Ga(0.47) As	p^+	$5x10^{18}$

p^+ cladding	300	Al0.85Ga0.15As(0.56)Sb(0.44)	p^+	2×10^{18}
i absorption	100	Al0.85Ga0.15As(0.56)Sb(0.44)	i	10^{15}
n^+ cladding	100	Al0.85Ga0.15As(0.56)Sb(0.44)	n^+	2×10^{18}
n^+ contact	1000	In (0.47) Ga As	n^+	5×10^{18}
Sustrate	---	InP	SI	---

9. Appendix 2: Scientific literature and sources for wet etching study

Chemical etchant 1	**Chemical etchant 2**	**Chemical etchant 3**	**References**
H2SO4:H2O2:H2O(1:8:80)	HCl(pure)	H2SO4:H2O2:H2O(1:8:80)	Our Experience
H2SO4:H2O2:H2O(1:8:80)	HCl:H2O(1:1)		Our Experience
H2SO4:H2O2:H2O(1:8:80)	HCl:H2O2:H2O(1:1:5)	H2SO4:H2O2:H2O(1:8:80)	[1] J. J. Xie, "Characterization of low noise InGaAs/AlAsSb Avalanche Photodiodes", PhD thesis, University of Sheffield, 2013.
H2SO4:H2O2:H2O(1:8:80)	HCl:H2O2:H2O(1:1:5)	HBr:C2H4O2:K2Cr2O7	Shiyu Xie Thesis
H3PO4:H2O2:H2O:Tartaric Acid (1ml:1ml:350ml:0.4g)			Appl. Phys. Lett. 75, n 18. D.K. Johnstone
H2SO4:H2O2:H2O(1:8:80)	H3PO4:H2O2:H2O:Tartaric Acid (1ml:1ml:350ml:0.4g)		Appl. Phys. Lett. 75, n 18. D.K. Johnstone
H2SO4:HCl:H2O(1:1:8)			Appl. Phys. Lett. 71, 1373 (1997); doi: 10.1063/1.119898
H3PO4:H2O2:H2O(3:4:15)	HCl:H2O2:H2O(1:1:5)		Our Experience
H2SO4:H2O2:H2O(1:8:80)	HCl:H2O2:H2O(1:1:5)	HCL:H2O2:H2O (1:1:60)	Our Experience

H2SO4:H2O2:H2O(1:8:80)	HCL:H2O2:H2O (1:1:60)		Our Experience
H2SO4:H2O2:H2O(1:8:80)	HCL:H2O2:H2O (1:1:60)		Our Experience
H2SO4:HCl:H2O(1:1:8)			Appl. Phys. Lett. 71, 1373 (1997); doi: 10.1063/1.119898
H2SO4:HCl:H2O(1:1:8)			Appl. Phys. Lett. 71, 1373 (1997); doi: 10.1063/1.119898
H2SO4:HCl:H2O(1:1:16)			Appl. Phys. Lett. 71, 1373 (1997); doi: 10.1063/1.119898
NH4(19:1)OH:H2O2:H2O(1:10:100)			Our Experience
H2SO4:H2O2:H2O(1:8:30)			Our Experience
HBr:HNO3:H2O(1:1:30)			N/A
HBr:HNO3:H2O(1:1:10)			N/A
H2SO4:H2O2:H2O(1:8:80)	HCl:H2O2:H2O(1:1:5)		Our Experience
H2SO4:H2O2:H2O(1:8:80)	HCl:H2O2:H2O(1:1:5)		Our Experience
H2SO4:H2O2:H2O(1:8:80)	HCl:H2O2:H2O(1:1:5)		Our Experience

H2SO4:H2O2:H2O(1:8:80)	HCl:H2O2:H2O(1:1:5)	HBr:C2H4O2:K2Cr2O7	Our Experience
H2SO4:H2O2:H2O(1:8:80)	HCl:H2O2:H2O(1:1:5)	HBr:C2H4O2:K2Cr2O7	Our Experience
H2SO4:H2O2:H2O(1:8:80)	HCl:H2O2:H2O(1:1:5)		Our Experience
H2SO4:H2O2:H2O(1:8:80)	HCl:H2O2:H2O(1:1:5)		Our Experience
H2SO4:H2O2:H2O(1:8:80)	HCl:H2O2:H2O(1:1:5)	H2SO4:H2O2:H2O(1:8:80)	Our Experience

10. Appendix 3: Scientific literature and sources for dry etching study

Compound	Etching	Gas	Rate	Comments	References
GaSb AlGaAsSb	ICP ICP ICP ICP	BCl3/Ar Cl2/Ar2 BCl3/Ar Cl2/Ar2	5100A/min 4.6μm/min 4200A/min	Info for RF Power/DC Bias/Pressure/Gas. Percentage can be found in the paper.	J.Vac.Sci.Technol. B 17(3), May/June 1999, pp965-969
GaSb AlGaAsSb InGaAsSb	ICP ICP ICP	BCl3/SiCl4 BCl3/SiCl4 BCl3/SiCl4	4μm/min 4μm/min 2.4μm/min	Photoresist: AZ 4330, positive, 3μm (etching <10μm). Photoresist: AZ 4903, positive, 17μm (etching ~90μm). Pre-etch step: Ar, 2mins, ICP power (100W), DC Bias (250W), 3sccm, 1.0Pa to remove native oxides->smooth and uniform etch profile. Second-etch step: BCl3/SiCl4.	Thin Solid Films 516 (2008) pp8712-8716
GaSb GaSb GaSb	ICP ICP ICP	Cl2/Ar2 Cl2/H2 Cl2/N2	2000-5000A/min	According to the paper, in order to use Cl2/N2, Cl2/H2, we need 750W for ICP power. Maximum limit in our clean room: 450W.	Materials Science in Semiconductor Processing 1 (1998) pp65-73
InGaAsSb/AlGaAsSb	ICP	Cl2/Ar	<20nm/min	Slow rate for GaSb-based quaternary alloys.	APL Vol.77, Number7, 2000, pp1008-1010
GaSb/AlGaAsSb/InGaSb/AlGaAsSb	RIE	BCl3			APL Vol.75, Number18, 1999, pp2779-2881
InGaAs/AlAsSb	ICP	SiCl4/Ar	1.2μm	RF Power: 220W, ICP Power: 100W, Gas Ratio 8/30	[1] J.J.Xie, "Characterization of low noise InGaAs/AlAsSb Avalanche Photodiodes", PhD thesis, University of Sheffield, 2013.
InGaAs/AlAsSb	ICP	Cl2/Ar	0.33μm/min	RF Power: 280W, ICP Power: 500W, Gas Ratio 7/12	[1] J.J.Xie, "Characterization of low noise InGaAs/AlAsSb Avalanche Photodiodes", PhD thesis, University of Sheffield, 2013.

11. Appendix 4: Fitted values from the C-V measurement of the Al(1-x)Ga(x)AsSb PIN diodes (M433x samples)

Wafer	Thickness (nm)	Composition	Doping (cm-3)		Growth notes	Fitted Doping (cm-3)	Fitted Thickness (nm)
M4333	100	In0.53 Ga0.47 As	p	5.00E+18			
	300	Al As0.56 Sb0.44	p	2.00E+18		2E+18	
	100	Al As0.56 Sb0.44	i	1.00E+15		1E+15	103
	100	Al As0.56 Sb0.44	n	2.00E+18		2E+18	
	1000	In0.53 Ga0.47 As	n	5.00E+18			
InP n-type (2-5)E+17							
M4335	100	In0.53 Ga0.47 As	p	5.00E+18			
	300	Al0.95 Ga0.05 As0.56 Sb0.44	p	2.00E+18		2.10E+18	
	100	Al0.95 Ga0.05 As0.56 Sb0.44	i	1.00E+15	As: 61%	1E+15	102
	100	Al0.95 Ga0.05 As0.56 Sb0.44	n	2.00E+18		2.4E+18	
	1000	In0.53 Ga0.47 As	n	5.00E+18			
InP n-type (2-5)E+17							
M4338	100	In0.53 Ga0.47 As	p	5.00E+18			
	300	Al0.9 Ga0.1 As0.56 Sb0.44	p	2.00E+18		2E+18	
	100	Al0.9 Ga0.1 As0.56 Sb0.44	i	1.00E+15	As: 66%	1E+15	99.5
	100	Al0.9 Ga0.1 As0.56 Sb0.44	n	2.00E+18		2E+18	
	1000	In0.53 Ga0.47 As	n	5.00E+18			
InP n-type (2-5)E+17							
M4339	100	In0.53 Ga0.47 As	p	5.00E+18			
	300	Al0.85 Ga0.15 As0.56 Sb0.44	p	2.00E+18		1.7E+18	
	100	Al0.85 Ga0.15 As0.56 Sb0.44	i	1.00E+15	As: 66%	1E+15	109
	100	Al0.85 Ga0.15 As0.56 Sb0.44	n	2.00E+18		1.7E+18	
	1000	In0.53 Ga0.47 As	n	5.00E+18			
InP n-type (2-5)E+17							